MATERIALS SCIENCE

Atomically dispersed Ni in cadmium-zinc sulfide quantum dots for high-performance visible-light photocatalytic hydrogen production

D. W. Su[1], J. Ran[2], Z. W. Zhuang[3], C. Chen[3], S. Z. Qiao[2]*, Y. D. Li[3]*, G. X. Wang[1]*

Catalysts with a single atom site allow highly tuning of the activity, stability, and reactivity of heterogeneous catalysts. Therefore, atomistic understanding of the pertinent mechanism is essential to simultaneously boost the intrinsic activity, site density, electron transport, and stability. Here, we report that atomically dispersed nickel (Ni) in zincblende cadmium–zinc sulfide quantum dots (ZCS QDs) delivers an efficient and durable photocatalytic performance for water splitting under sunlight. The finely tuned Ni atoms dispersed in ZCS QDs exhibit an ultrahigh photocatalytic H_2 production activity of 18.87 mmol hour^{-1} g^{-1}. It could be ascribed to the favorable surface engineering to achieve highly active sites of monovalent Ni(I) and the surface heterojunctions to reinforce the carrier separation owing to the suitable energy band structures, built-in electric field, and optimized surface H_2 adsorption thermodynamics. This work demonstrates a synergistic regulation of the physicochemical properties of QDs for high-efficiency photocatalytic H_2 production.

INTRODUCTION

The design of catalysts with suitable chemical and physical properties is essential for many energy conversion and storage technologies, such as water electrolyzers, photocatalytic water splitting, metal-air batteries, and fuel cells. Introducing active single atoms into the catalysts has been the most widely used strategy to tune the electronic structure of the catalysts to optimize their intrinsic activities, electronic transport, active site densities, and stability (*1*–*3*). Furthermore, downsizing catalyst particles or clusters to single atoms is highly desirable for maximizing catalytic efficiency. It has been well recognized that the isolated active atoms singly dispersed in matrices can maximize the efficiency of atom utilization (hence, single-atom catalysts) in acidic (*4*) and alkaline (*5*) hydrogen evolution reaction (HER) (*6*), electrochemical reduction of CO_2 (*7*), CO oxidation (*2*), etc.

The structurally uniform and well-defined single atomic sites in a simple structure provide atomic-level insight and the corresponding catalytic reaction mechanism (*2*, *8*, *9*). However, it is still a big challenge to understand the catalytically active center in "atomic interfaces" (typically with different charges or even different chemical identities) (*7*) within higher complexities. Obviously, the identification of an active site structure with more sophisticated functionalities is crucial for catalytic reactions that simultaneously require different kinds of functional active sites. Grimaud and Xu *et al.* (*10*) found that substituting Al of inactive but low-cost $CoAl_2O_4$ with a small amount of Fe can activate the preoxidation of Co and optimize the O 2p level of oxide for greater structural flexibility to facilitating the surface reconstruction of $CoAl_2O_4$. They revealed that on the reconstructed surface, the Fe substitution facilitates a two-step deprotonation process, which leads to the formation of active oxygen sites at a low overpotential and thus greatly promotes the oxygen evolution reaction (OER) (*10*). The $Cd_{1-x}Zn_xS$ solid solution rather than bare CdS and ZnS demonstrated efficient photocatalytic properties for hydrogen (H_2) evolution in the presence of sacrificial electron donors. Its photocatalytic activities can be optimized by adjusting the *x* value for achieving appropriate band structure for the photocatalytic H_2 production (*11*–*13*). Xu and Wang *et al.* (*14*) also unveiled the accurate amount of catalytically inactive Zn^{2+} incorporating into CoOOH that can give rise to oxygen nonbonding states with different local configurations, which is critical to regulating the OER mechanism. They found that if two neighboring nonbonding oxygens with the partially filled O(2p) band can hybridize their oxygen holes without sacrificing metal-oxygen hybridization substantially, the OER proceeds via the lattice oxygen oxidation mechanism pathway on the metal oxyhydroxides, discovering that $Zn_{0.2}Co_{0.8}OOH$ has optimum activity (*14*). Identification of active site structures is even more vital for the photocatalytic H_2 production through water splitting driven by visible light because of their complex multiple reaction processes: from light harvesting to charge (electron and hole pairs) excitation, further to photocatalyst surface engineering for both HER and OER (*15*–*17*). Therefore, it is critical to investigate the efficiency of the introduced single atoms on a per-atom basis and further systematically evaluate the electronic and structural properties of the photocatalysts to realize synergetic integration of photocatalytic constituents into a functional heterostructure. One of the challenges to unveil the synergistic effect of the single atoms with their coordinating elements is the irregular structure of the bulk catalysts, resulting in the different exposed facets with anisotropic physical and chemical properties.

In contrast to the elusive irregular bulk materials, here we use a crystallographic and structural chemistry design approach to manipulate the atomically dispersed nickel (Ni) in zincblende cadmium–zinc sulfide quantum dots (ZCS QDs), maximizing the photocatalytic properties for water splitting driven by visible light. The colloidal QDs, such as ZnS-coated InP QDs (*15*) with tunable bandgap and versatile surface properties, remain among the most promising photocatalysis for the HER. Here, experimental investigation and theoretical density function theory (DFT) calculations revealed that with continuous adjustment on the concentration of atomically dispersed

[1]Centre for Clean Energy Technology, School of Mathematical and Physical Sciences, Faculty of Science, University of Technology Sydney, Ultimo, NSW 2007, Australia. [2]School of Chemical Engineering and Advanced Materials, The University of Adelaide, Adelaide, SA 5005, Australia. [3]Department of Chemistry, Tsinghua University, Beijing 100084, China. *Corresponding author. Email: guoxiu.wang@uts.edu.au (G.X.W.); s.qiao@adelaide.edu.au (S.Z.Q.); ydli@mail.tsinghua.edu.cn (Y.D.L.)

Ni, the anisotropy of different crystalline facets [(111) and (110)] of the ZCS QDs can be fine-tuned. In particular, the (111) facets consisting of isolated, high-density, low-valence Ni(I) as verified by the x-ray absorption fine structure analysis (XAFS), electron energy-loss spectroscopy (EELS) spectra, etc., show a highly catalytic activity for HER. Furthermore, surface heterojunctions due to the different exposed crystal planes [(111) and (110)] in the same phase maximize the charge carrier separation. Meanwhile, the built-in electric field (BIEF) can further facilitate the charge carrier migration to the surface, leading to enhanced electronic conductivity. Together with proper surface H_2 adsorption thermodynamics on the atomically dispersed Ni(I) active sites, the optimized $Ni_{0.03125}Zn_{0.25}Cd_{0.75}S$ QDs achieved a remarkable photocatalytic H_2 production rate of 18.87 mmol hour^{-1} g^{-1}. This work could pave a new avenue for the synergistic modulation of the physicochemical properties of nanocrystals to substantially improve their performances for various applications, e.g., catalysis, electronics, and optoelectronics.

RESULTS AND DISCUSSION

Phase structures and morphology

Stoichiometric ZCS QDs were synthesized through the hot injection approach, using metal chloride and thioacetamide (TAA) as precursors and oleylamine (OLA) as the reducing and stabilizing agent. The field emission scanning electron microscopy (FESEM), the high-resolution transmission electron microscopy (HRTEM), and the high-angle annular dark field scanning TEM (HAADF-STEM) images were used to identify the morphology of the as-prepared QDs. It shows that the monodisperse ZCS QDs with the uniform tetrahedral shape and a narrow size distribution (~8.5 nm) were obtained (fig. S1, A to D). They exhibit an equilateral triangle shape with a 60° angulus parietalis, and the fast Fourier transform (FFT) plots can be indexed as (111) crystal planes of the zincblende structure (fig. S1, E to G). The ZCS QDs are enclosed by (111) facets, as identified by the angles of the simulated outlines of the triangular pyramids sitting on the tetrahedral facets together with the HAADF-STEM (fig. S1, H to L). After dispersing Ni into ZCS QDs, we obtained four Ni_xZCS (x = 0.015625, 0.03125, 0.0625, and 0.125) QDs. All these QDs are monodisperse (with an average size of ~8.0 nm). They self-assemble to form a superlattice structure (Fig. 1, A_1 to D_1 and A_2 to D_2, and fig. S2, A to H), as confirmed by the regular hexagonal arrangement FFT patterns (insets of Fig. 1, A_1 to D_1). The low polydispersity in size can be ascribed to the temperature-dependent release of reactive sulfur species from TAA and the optimized reactivity of metal-OLA complexes, which facilitates the better separation of nucleation and growth stages (fig. S2, I to R) (*18*). With increasing Ni content, the color of the as-prepared QDs gradually changes from yellow to dark green (fig. S2, S to W), indicating the composition variation over the entire series. The HAADF-STEM images (Fig. 1, A_3 to D_3) show that the vertices of the tetrahedra are truncated with ~120° facets, and the vertices become more truncated with increased Ni in Ni_xZCS QDs, resulting in the shape evolution from tetrahedra to truncated tetrahedra as demonstrated by the geometrical models (Fig. 1, A_6 to D_6). The FFT patterns (Fig. 1, A_5 to D_5) of the atomically resolved HAADF-STEM images (Fig. 1, A_4 to D_4) verify their dominant (111) facets. Moreover, the Miller indices of the angulus parietalis on facets of the truncated tetrahedra are determined through analyzing the projection angles (*19*). It proves that only the (110) cobundled facets can contribute to 120° angulus parietalis for the truncated tetrahedral architecture (fig. S2X). Therefore, the as-prepared $Ni_xZn_{0.25}Cd_{0.75}S_{1+x}$ QDs are enclosed by the (111) and (110) facets only. Figure S3 shows more detailed shape evolution images of the Ni_xZCS QDs along [111], [100], [110], and [112] orientations, confirming the role of Ni in the evolution of the enclosed facets. For comparison, the bare CdS and ZnS QDs were also synthesized through the same process. They also present the uniform size distribution and the tetrahedral morphology (fig. S2, Y and Z). As characterized by FESEM, HRTEM, and HAADF-STEM, it confirms the uniform size, surface morphology, and crystallography of the as-prepared Ni_xZCS QDs. Furthermore, the clearly identified anisotropy crystal facets of the Ni_xZCS QDs could present the tunable electron structure to tune the photocatalytic activity.

To gain deeper insight into the phase structures of the bulk and surface compositions of the Ni_xZCS QDs, inductively coupled plasma mass spectrometry (ICP-MS), energy-dispersive x-ray spectroscopy (EDS), the Rietveld refinement x-ray diffraction (XRD) patterns, and the selected area electron diffraction (SAED) analyses were explored. ICP-MS and EDS measurements confirm that the chemical compositions of Ni_xZCS QDs are close to the molar ratio of Ni, Zn, and Cd in the initial solution (table S1). Owing to the similar covalent radii of Ni, Zn, and Cd (121, 131, and 148 pm, respectively), Zn and Ni can readily substitute Cd within the Ni_xZCS QDs, which was confirmed by the calculated lowest free energy of the substitute dopants (fig. S4, A to G, and table S2). Moreover, the formation energy of an impurity Ni is 0.45 eV in the $Ni_{0.125}ZCS$ when nickel chloride is used as Ni source, implying the high solubility of Ni in the ZCS matrix. This is also identified by the Rietveld refinement XRD patterns (fig. S4, H to L). The lattice parameters decreased from 5.712 Å for bare ZCS QDs to 5.706, 5.694, 5.665, and 5.631 Å for Ni_xZCS (x = 0.015625, 0.03125, 0.0625, and 0.125) QDs, respectively, which is well consistent with the DFT calculation results and Vegard's law plot (fig. S4, M and N) (*20*). The main XRD peaks [(111), (220), and (311)] continuously shift toward higher angles without phase separation along with increasing Ni content, indicating the homogeneous structure of the Ni_xZCS solid solutions (fig. S4l). As calculated (fig. S4, O to S), with Zn and Ni substitute, the T_d symmetry of the [CdS_4] tetrahedron is preserved, but the atomic relaxation results in an isotropic elongation of the four Cd—S bonds, indicating that the [Ni/ZnS_4] tetrahedron experiences a local inward relaxation with shorter Ni—S and Zn—S bond length (~2.33 Å) than the original Cd—S bond (~2.53 Å). It implies the effect of the atomically dispersed Ni on the volume shrinkage of the supercell along with increasing Ni content. The SAED ring patterns are consistent with XRD results (fig. S4, T to W). Together with the ICP-MS and EDS measurements, it elucidates the solid solution feature of the as-prepared Ni_xZCS QDs, which could benefit the electron conductivity for their catalytic applications.

Depth profiling of the crystal structure and electronic structure was carried out using x-ray photoelectron spectroscopy (XPS). The atomic ratios of Ni/Zn/Cd on the surface are 3.13%:28.18%:68.69%, 9.50%:26.71%:63.79%, 11.75%:23.23%:65.02%, and 12.65%:21.53%:65.82% for Ni_xZCS (x = 0.015625, 0.03125, 0.0625, and 0.125) QDs, respectively, as measured by XPS. The metal versus S ratio was confirmed to be around 62%:38%, indicating the loss of the S on the surface. The dangling S on the (111) crystal plane of zincblende presents a much higher activity, implying their instability [~2 eV higher surface energy of (111) facets with dangling S than the one without dangling S]. The high-resolution XPS results of Zn 2p and Cd 3d agree well with

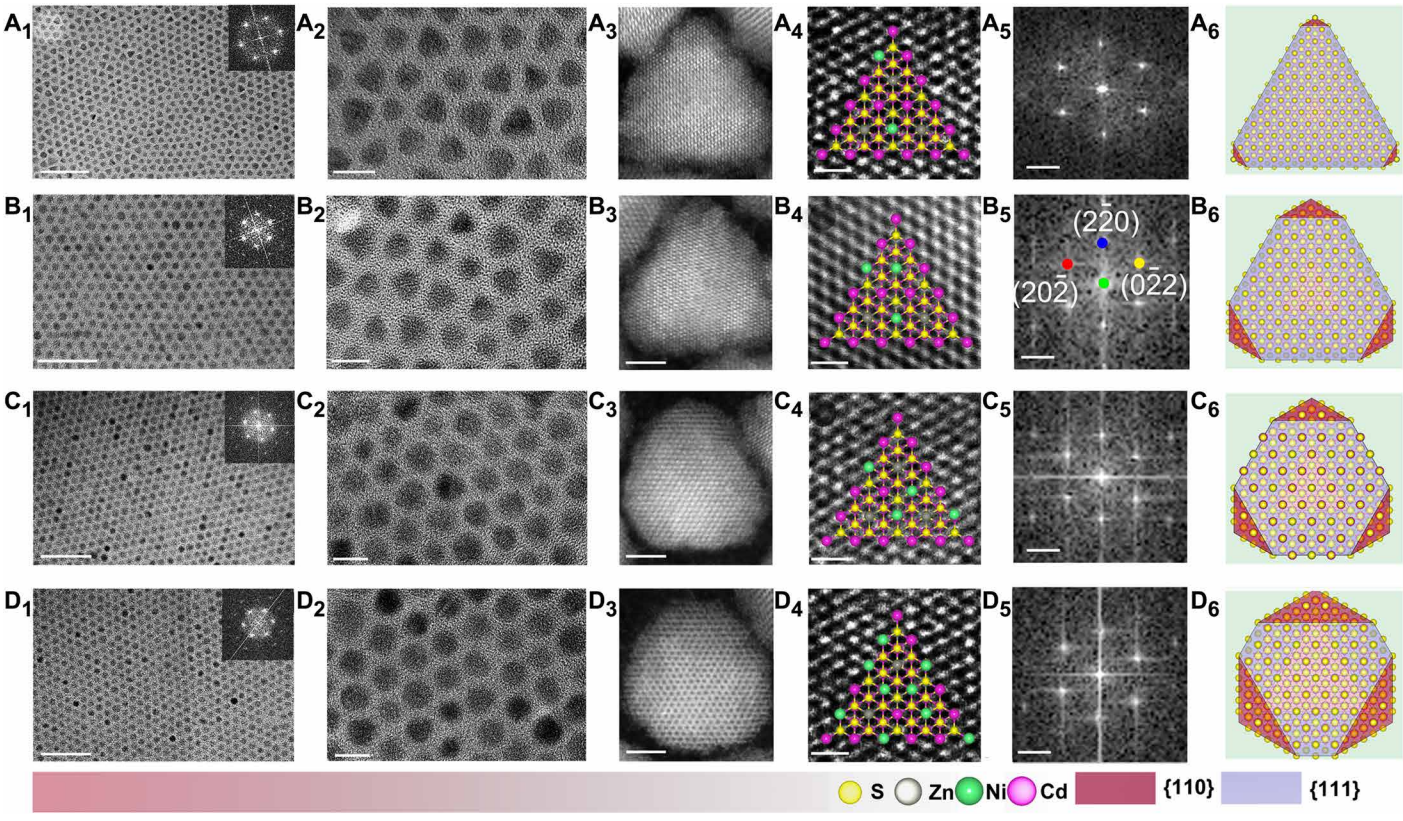

Fig. 1. Morphologies of the metal sulfide QDs. TEM (**A_1**, **B_1**, **C_1**, and **D_1**), HRTEM (**A_2**, **B_2**, **C_2**, and **D_2**), and HAADF-STEM (**A_3**, **B_3**, **C_3**, and **D_3**) images of Ni_xZCS ($x = 0.015625$, 0.03125, 0.0625, and 0.125) QDs. (**A_4**), (**B_4**), (**C_4**), and (**D_4**) are atomically resolved HAADF-STEM images of the typical freestanding Ni_xZCS QDs viewed along the [111] orientation, and (**A_5**), (**B_5**), (**C_5**), and (**D_5**) are their corresponding FFT patterns. (**A_6**), (**B_6**), (**C_6**), and (**D_6**) are the simulated atomic models of the as-prepared Ni_xZCS ($x = 0.015625$, 0.03125, 0.0625, and 0.125) QDs. Insets in (A_1) to (D_1) are the FFT patterns of the TEM images, showing their regular hexagonal arrangement. Insets in (A_4) to (D_4) are the simulated atom arrangement of the (111) crystal planes of the zincblende structure. Scale bars, 50 nm (A_1, B_1, C_1, and D_1), 10 nm (A_2, B_2, C_2, and D_2). 2 nm (A_3, B_3, C_3, and D_3), 5 Å (A_4, B_4, C_4, and D_4), and 5 1/nm (A_5, B_5, C_5, and D_5).

the values reported for the divalent Zn and Cd in pure metal sulfides (fig. S5, A and B) (*21*, *22*). Two subpeaks in S 2p 3/2 XPS spectra (Fig. 2A) can be ascribed to the lattice S^{2-} (at ~161.1 eV) and the oxidized states of S (at ~163.2 eV), respectively (*23*). The gradually decreased subpeak at ~162.9 eV indicates the lower oxidization of surface S along with increased concentration of Ni in Ni_xZCS QDs. This is consistent with the geometry evolution of the Ni_xZCS, because more (110) facets increase the Bader charge of surface S [−0.92 to −0.96 V for (110) facets and −0.85 to −0.91 V for (111) facets, table S3]. The Ni 2p XPS profile shows the main peaks of Ni $2p_{3/2}$ and Ni $2p_{1/2}$ at ~855.3 and ~872.6 eV, respectively (Fig. 2B) (*24*). The former main peak can be ascribed to the direct charge transfer from the nearest-neighbor S 2p to Ni core hole (*25*, *26*). It can be fitted into a doublet (~855.6 and ~856.9 eV, peaks 1 and 2) with the increased Ni concentration, which is related to the two different photoemission channels: e.g., a single Ni site screened by a shift of electron density from the surrounding nearest-neighbor S 2p (peak 1) and a nonlocal effect from an adjacent cation occupancy (peak 2) (*27*). Here, peak 2 can only be ascribed to the adjacent Ni cation occupancy, which is evidenced by the local density of state (LDOS) of the Ni, Zn, Cd, and S in the Ni_xZCS (fig. S5, C to F). The d10 metals Cd and Zn show a tight and localized DOS at the bottom edge of the valence band (VB) in Ni_xZCS crystals and do not participate in bonding. Only Ni 3d levels occupied the top of the VB and bottom of the conduction band (CB), together with substantial S 2p charge-transfer character to form the bandgap. It indicates that Ni 2p3/2 peak 2 can only be derived from the adjacent Ni nonlocal effect. Thus, owing to the low Ni concentration within $Ni_{0.015625}ZCS$ and $Ni_{0.03125}ZCS$ QDs, the adjacent Ni nonlocal screening is eliminated, resulting in the broader peak 2 within Ni 2p3/2 peaks, which is hard to distinguish, compared with the ones in the higher Ni doping levels samples. Furthermore, the $2p^53d^8$ state associates with the satellite feature, leading to the broad peak at ~863 eV, which agrees with the single metal site character even for very dilute Ni (*28*). Such broad satellite peak also decreased in Ni_xZCS QDs within less Ni because of the less Ni d-d nonlocal screening transition contributions (*25*, *26*), confirming the low-level Ni distribution within the $Ni_{0.015625}ZCS$ and $Ni_{0.03125}ZCS$ QDs. As revealed by the XPS, the Ni atoms are highly uniformly distributed within the Ni_xZCS QDs host crystals, which can benefit the usage of Ni active sites.

To further probe the local hybridization states of Ni in the Ni_xZCS QDs on high spatial resolution down to the nanometer level, the L-edge EELS was collected to measure the Ni dipole transitions from 2p orbitals to unoccupied 3d orbitals. The L-edge EELS was recorded to evaluate the local electron distributions and magnetic moments of Ni (Fig. 2C) (*29*, *30*). The L_3/L_2 white-line ratio of Ni is increased from 1.124 for $Ni_{0.015625}ZCS$ to 1.21 for $Ni_{0.03125}ZCS$, 1.420

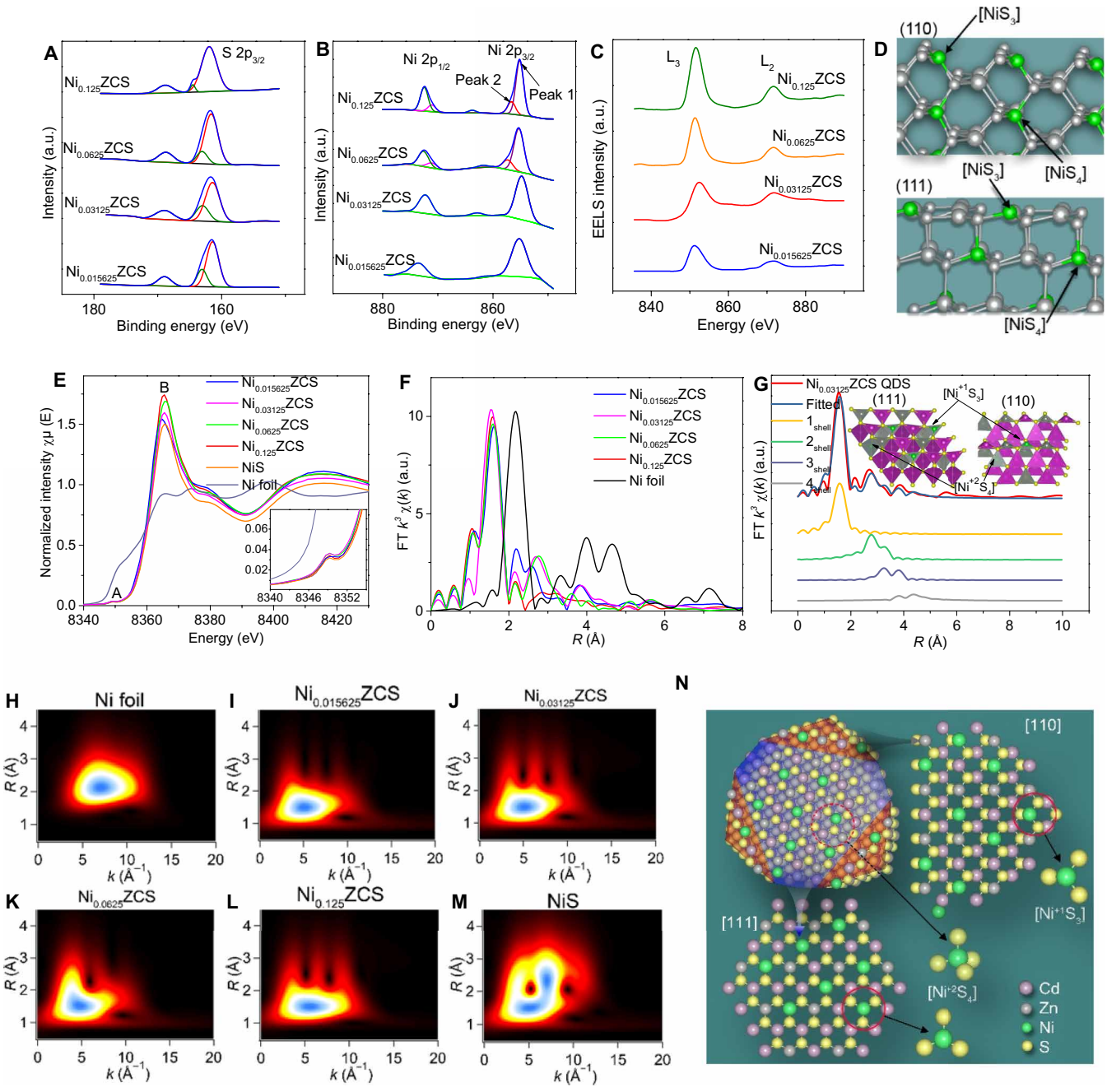

Fig. 2. Physicochemical characterization of the Ni_xZCS QDs. High-resolution S 2p spectra (**A**) and Ni 2p spectra (**B**) of Ni_xZCS QDs ($x = 0.015625$, 0.03125, 0.0625, and 0.125). The XPS spectra are normalized to the Cd intensity. a.u., arbitrary units. (**C**) The EELS spectra of Ni in the Ni_xZCS ($x = 0.125$ 0.03125, 0.0625, and 0.125) QDs. (**D**) Schematic diagraph of (111) and (110) facet crystals. (**E**) The Ni K-edge XANES spectra of Ni_xZCS ($x = 0.015625$, 0.03125, 0.0625, and 0.125) QDs, where peak A represents 1s → 3d transition and peak B represents 1s → 4p transition (the inset shows the expanded pre-edge region). (**F**) Fourier transform [$k^3\chi(k)$] of the phase-uncorrected extended x-ray absorption fine structure spectra (EXAFS) of Ni_xZCS ($x = 0.015625$, 0.03125, 0.0625, and 0.125) QDs. (**G**) Four-shell fitting of Fourier transformations of EXAFS spectra for $Ni_{0.03125}ZCS$. EXAFS spectra were fitted using the FEFF 8.0 code [the inset shows the structure of the Ni site in DFT optimized (111) and (110) facet crystals; the balls in green, gray, purple, and yellow represent Ni, Zn, Cd, and S atoms, respectively]. (**H** to **M**) Wavelet transform plots of Ni foil, Ni_xZCS ($x = 0.015625$, 0.03125, 0.0625, and 0.125) QDs, and NiS. (**N**) Schematic diagraph of the crystal structures of the as-prepared Ni_xZCS ($x = 0.015625$, 0.03125, 0.0625, and 0.125) QDs.

for $Ni_{0.0625}ZCS$, and 1.573 for $Ni_{0.125}ZCS$ QDs, indicating the gradually lowered occupied Ni d orbit and more unpaired electrons (enhanced magnetic moments) within Ni (*29*, *30*). We studied the anisotropy crystal facets of the orthorhombic nonpolar (110) surface and hexagonal polar (111) surfaces of the Ni_xZCS to reveal the local electronic structure of Ni in Ni_xCZS QDs. As confirmed by both surface energy and experimental M:S molar ratio results (XPS and EDS, table S1), the metal cations on the polar (111) surface

coordinate with three S rather than four. The relaxed top MS (M = Ni, Zn, and Cd) layers of both (111) and (110) crystal planes appear corrugated with respect to the bulk termination, and all cations in the outermost layer tend to downshift toward the inner layer (S tends to upshift) (Fig. 2D and fig. S5, G and H). The Ni and Zn ions become almost coplanar with their three coordinated S atoms (Cd even further downshifts to form the invagination pyramid), and shorter M—S bond lengths (~2.25 Å for both Zn—S and Ni—S and ~2.48 for Cd—S) were achieved. The (111) surfaces demonstrated a flatter feature (almost parallel to the *ab* plane) than the (110) ones (~137° to the *ab* plane). Being consistent with the Bader charge [0.95 to 0.98 for (110) and 0.54 to 0.58 for (111) facets] and the unpaired electron number of Ni [1.61 to 1.69 for (110) and 0.95 to 0.99 for (111) facets], the magnetic moments of Ni atoms were calculated to be 1.61 to 1.69 μ_B for (110) facets and 0.95 to 0.99 μ_B for (111) facets (table S4). These results unveil that the Ni in the (111) facets shows one unpaired electron with a $3d^9$, $S = 1/2$ electronic configuration and monovalent oxidation state, whereas the Ni in (110) facets features two unpaired electrons and a $3d^8$, $S = 2/2$ electronic configuration. Therefore, as characterized by the Ni EELS spectra, the higher L_3/L_2 white-line ratio derived from more Ni dipoles transitioning from 2p to 3d orbits can be ascribed to the more unoccupied Ni 3d orbits on the (110) facets. Meanwhile, as unveiled by the EELS, the unpaired electrons on the (110) and (111) facets can contribute to more interaction with the H.

The localized coordination environments of induced Ni within Ni_xZCS QDs crystals were confirmed by the XAFS (Fig. 2, E to M). All four K-edge Ni x-ray absorption near-edge structure (XANES) spectra present the prepeak at ~8348 eV (peak A in Fig. 2E), suggesting the dipole-forbidden but quadrupole-allowed transition and the 3d empty metal states and 4p orbit hybridization of the Ni central atoms (*31*). Furthermore, along with the increase of Ni in Ni_xZCS QDs, the pre-edge peak intensity increased (inset of Fig. 2E), indicating the more empty p component in p-d hybridized orbits. These are consistent with the EELS spectra that presented more (110) facets, resulting in the less occupied p component. Figure S6 simulated the XANES of NiS_x ($x = 6$, 4, and 3) complexes to study their symmetrical dependency. The shoulder near 8348 eV appears in the sixfold coordinated NiS_6 octahedron (O_h), fourfold coordinated NiS_4 tetrahedra (T_d), threefold coordinated NiS_3 triangular pyramid, and the trigonal planar complex (C_{3v}), but not in the square planar complexes (C_{4v}) (*32*). For NiS_6 O_h symmetry, the e_g (d_z^2 and $d_{x^2-y^2}$) mainly contributes to the electric dipole and quadrupole transitions, whereas for the NiS_4 T_d, it mainly comes from the t_{2g} (d_{xy}, d_{yz}, and d_{xz}) (fig. S6, A to C). Losing one more axial to form the threefold coordinated NiS_3 triangular pyramid, it presented a more intense pre-edge peak, mainly contributed by e_g, and the intensity increased along with the Ni moving toward the planar center, reaching the maximum with the trigonal planar complex (C_{3v}). This is consistent with the pre-edge peak intensity changing from $Ni_{0.125}$ZCS to $Ni_{0.015625}$ZCS QDs. These transitions can serve as a fingerprint for identifying the trigonal planar Ni-S_3 (*25*, *29*). After calculation of the two shells [NiS_4M_{12} and NiS_3M_9 for (111) facets and NiS_3M_7 for (110) facets, fig. S6D], the calculated XANES of NiS_4M_{12} presented the highest white line (1s → 4p dipole transfer) and NiS_3M_9 mainly contributed to the prepeak (1s → 3d transfer). The experimental XANES of Ni_xZCS QDs shows higher white line intensity than Ni foil and NiS. The intensities were enhanced with increased Ni in Ni_xZCS QDs, confirming the Ni_xZCS QDs mixed with the threefold coordinated NiS_3 and fourfold coordinated NiS_4 tetrahedra (T_d). Furthermore, the XANES edge positions of Ni_xZCS QDs lie between those of Ni foil and NiS, indicating that their oxidization state is between 0 and +2 (inset in Fig. 2E). This also confirms the Ni mixed with the threefold coordinated NiS_3 and T_d symmetry as demonstrated in Fig. 2D. Figure 2F displays the Fourier transform (FT) $k^3\chi(k)$ of the phase-uncorrected extended x-ray absorption fine structure spectra (EXAFS). The FT $k^3\chi(k)$ of Ni foil displays peak at 2.15 Å, corresponding to Ni-Ni interaction and does not appear in any of the Ni_xZCS QDs, confirming isolation of Ni in Ni_xZCS QDs. The main peak at ~1.58 Å of Ni_xZCS QDs is attributed to the scattering interaction between Ni and the first shell S (Ni-S). Figure 2G and fig. S6 (E to G) show the four-shell fitted FT $k^3\chi(k)$ EXAFS spectra of $Ni_{0.03125}$ZCS QDs and Ni_xZCS ($x = 0.015625$, 0.0625, and 0.125) QDs, respectively. It is well matched with DFT-optimized (111) and (110) facet crystals (inset of Fig. 2G and table S5 summarize the fitting results). The wavelet transform plot of Ni foil shows the maximum at around 7 $Å^{-1}$ (Fig. 2H), corresponding to Ni—Ni bonding, while for NiS, there are two wavelet transform plot maximal centers, related to Ni—S (5 $Å^{-1}$) and Ni—Ni (7 $Å^{-1}$) bonding, respectively (Fig. 2M). The maximum wavelet transforms of Ni_xZCS QDs are all around 5 $Å^{-1}$ (Fig. 2, I to L), aligning with Ni—S bonding only. All these XAFS results elucidate that the Ni coordinates with the threefold S on (110) and (111) surfaces and fourfold S within the T_d symmetry, suggesting the different localized electron structures on the surface, profiting the tunable catalytic property, as illustrated in Fig. 2N. Furthermore, DFT calculations on surface energy and the adsorption energies of OLA on the crystal planes (fig. S3, I and J) were applied for disclosing the morphology evolution on Ni_xZCS ($x = 0.015625$, 0.03125, 0.0625, and 0.125) QDs, as shown in fig. S3 (E to L).

The sub-angström-resolution aberration-corrected HAADF-STEM and corresponding STEM-EDS spectrum were conducted to observe the highly uniformly distributed Ni atom within the Ni_xZCS host crystals. The clean surfaces and edges of the Ni_xZCS QDs can be observed by the HAADF-STEM (Fig. 3, A to D). The STEM-EDS elemental mapping of the $Ni_{0.03125}$ZCS QDs readily reveals the homogeneous distribution of Ni, Zn, Cd, and S in the integrated QDs (Fig. 3, E to H). HAADF images represent the projection of atoms along the incident beam direction. Therefore, the sub-angström-resolution aberration-corrected HAADF-STEM images of Ni_xZCS ($x = 0.015625$, 0.03125, 0.0625, and 0.125) QDs along the [111] zone axis with different intensities for atomic columns (Fig. 3, I to L) were used to characterize the dispersion and configuration of the Ni/Zn and Cd atoms on the basis of *Z*-difference of the individual heavy atoms (*33*). The individual Ni atoms occupy exactly the positions of the Cd and/or Zn atoms within the surface of Ni_xZCS QDs without the interstitial sites, which is comparable with the simulated Ni-substituted scanning tunneling microscope (STM) image of the (111) surface of $Ni_{0.03125}$ZCS (Fig. 3M). The line profiles (Fig. 3N) of the (111) surface of $Ni_{0.03125}$ZCS marked in Fig. 3J, showing different intensities, could identify the different elements (higher intensity represents Cd-rich atomic columns and lower intensity denotes Zn/Ni-rich atomic columns). The measured distances between two adjacent atoms (Fig. 3N) can be fitted with the relaxed Ni_xZCS crystals (fig. S6, H to J). The atomically resolved HAADF-STEM confirms the uniformly distributed Ni, Zn, and Cd in the as-prepared Ni_xZCS QDs, which can profit the catalytic properties.

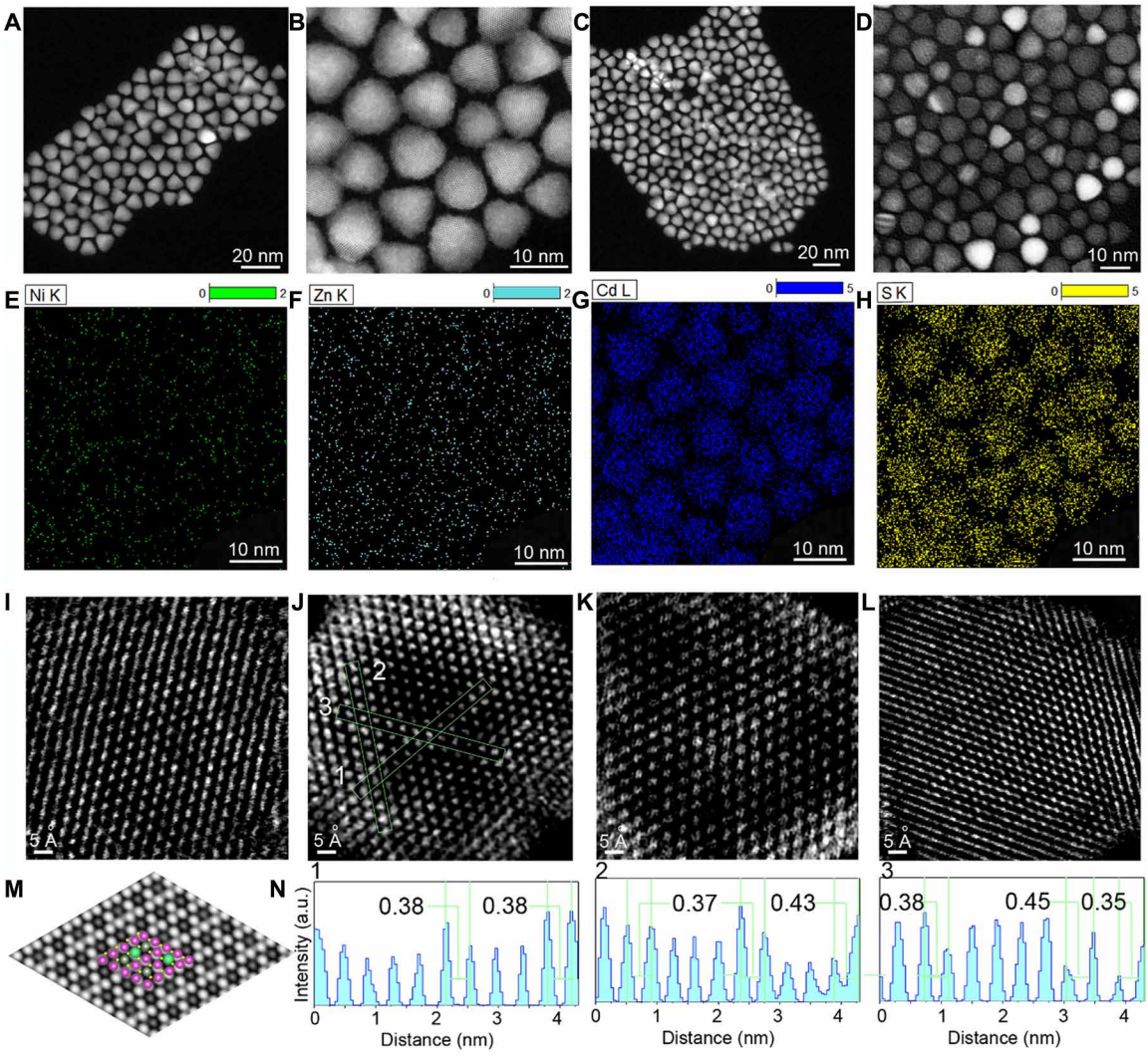

Fig. 3. HAADF-STEM and EDS spectrum. (**A** to **D**) Low-magnification HAADF-STEM images of $Ni_{0.015625}$ZCS QDs (A), $Ni_{0.03125}$ZCS QDs (B), $Ni_{0.0625}$ZCS QDs (C), and $Ni_{0.125}$ZCS QDs (D). (**E** to **H**) The EELS mapping of $Ni_{0.03125}$ZCS QDs. (E) S, (F) Ni, (G) Zn, and (H) Cd. (**I** to **L**) Sub-angström-resolution aberration-corrected HAADF-STEM images of Ni_xZCS (x = 0.015625, 0.03125, 0.0625, and 0.125) QDs along the [111] zone axis with different intensities for atomic columns: higher intensity for Cd-rich atomic columns and lower intensity for Zn/Ni-rich atomic columns; (I) $Ni_{0.015625}$ZCS QDs, (J) $Ni_{0.03125}$ZCS QDs, (K) $Ni_{0.0625}$ZCS QDs, and (L) $Ni_{0.125}$ZCS QDs. (**M**) Simulated scanning tunneling microscope (STM) image of the (111) surface of $Ni_{0.03125}$ZCS. The inset shows the corresponding atom arrangement along the [111] orientation. The yellow, dark pink, gray, and light gray colors represent the S, Cd, Zn, and Ni atoms, respectively. (**N**) Line profiles show the variation in intensities along the directions marked in (J).

Photocatalytic performances of H_2 production

The activity in the visible-light–powered photocatalytic H_2 evolution of Ni_xZCS QDs was evaluated (Fig. 4A). As comparison samples, the bare CdS and ZnS QDs have negligible visible-light photocatalytic activity with very limited H_2 production rates of 242 and 207 μmol $hour^{-1}$ g^{-1}, respectively. The ZCS QDs increase H_2 production rate to 1.50 mmol $hour^{-1}$ g^{-1}. The Ni_xZCS QDs show a remarkable enhancement of the H_2 production rates. In particular, $Ni_{0.015625}$ZCS QDs achieved a H_2 production rate of 13.74 mmol $hour^{-1}$ g^{-1}. With increasing Ni content, $Ni_{0.03125}$ZCS QDs present the optimal photocatalytic properties and obtained the highest H_2 production rate of 18.87 mmol $hour^{-1}$ g^{-1}, exceeding that of bare CdS QDs by a factor of 78- and 2.7-fold superior activity over the 1.9 weight % (wt %) Pt-loaded CdS QDs (6.88 mmol $hour^{-1}$ g^{-1}). The stability of the optimized $Ni_{0.03125}$ZCS QDs was further tested by cycling photocatalytic experiments (Fig. 4B). No substantial deterioration of photocatalytic activity was observed during cycling. A further increase in the Ni content led to deterioration of photocatalytic performance. $Ni_{0.0625}$ZCS and $Ni_{0.125}$ZCS QDs delivered a H_2 production rate of 12.11 and 6.97 mmol $hour^{-1}$ g^{-1}, respectively. The stability of the as-prepared $Ni_{0.03125}$ZCS QDs was further confirmed by the post-characterization via the STEM, EXAFS, and XPS after the cycling test (fig. S7). It can be seen that after the cycling test, the $Ni_{0.03125}$ZCS QDs still preserve the truncated tetrahedra shape with the well-defined crystalline feature (fig. S7, A to C). The QDs also mainly exposed with the (111) facets as verified by their corresponding FFT pattern analyses (fig. S7, D to F, taken from marked areas in fig. S7C). As confirmed by the high-resolution Ni 2p spectra of $Ni_{0.03125}$ZCS QDs after the cycling test (fig. S7G), the sharp Ni 2p3/2 peak and the broad satellite peak at ~863 eV associated with the $2p^5 3d^8$ state

agree with the single metal site character (*28*). Furthermore, the Ni K-edge XANES spectra and the corresponding EXAFS FT [$k^3\chi(k)$] spectra of $Ni_{0.03125}$ZCS QDs (fig. S7, H and I) after the cycling test are comparable with those of the fresh sample, identifying the Ni state as well as the surface composition as stable under photocatalytic conditions.

The light-harvesting capability, charge separation and transfer ability, and surface redox reactions were studied to understand the intrinsic photocatalytic property of Ni_xZCS QDs. Ultraviolet-visible (UV-vis) diffuse reflectance spectra show that the ZCS QDs have an absorption edge (~465 nm) between those of bare ZnS and CdS QDs (Fig. 4C). After Ni dispersion, a continuous red shift of the absorption edges can be observed [~469, ~476, ~500, and ~528 nm for Ni_xZCS QDs (x = 0.015625, 0.03125, 0.0625, and 0.125), respectively, Fig. 4C]. The bandgap of ZCS QDs was measured to be 2.75 eV, while Ni_xZCS QDs have gradually decreasing bandgaps of 2.72, 2.67, 2.56, and 2.42 eV, respectively (Fig. 4D). The calculated band structures of bulk CdS, ZnS, and ZCS are shown in fig. S8 (D to F), with bandgaps of 2.41, 3.53, and 2.71 eV, respectively, which are well consistent with the experimental results (Fig. 4D) and the previous reported results (*11*–*13*). They are larger than the values

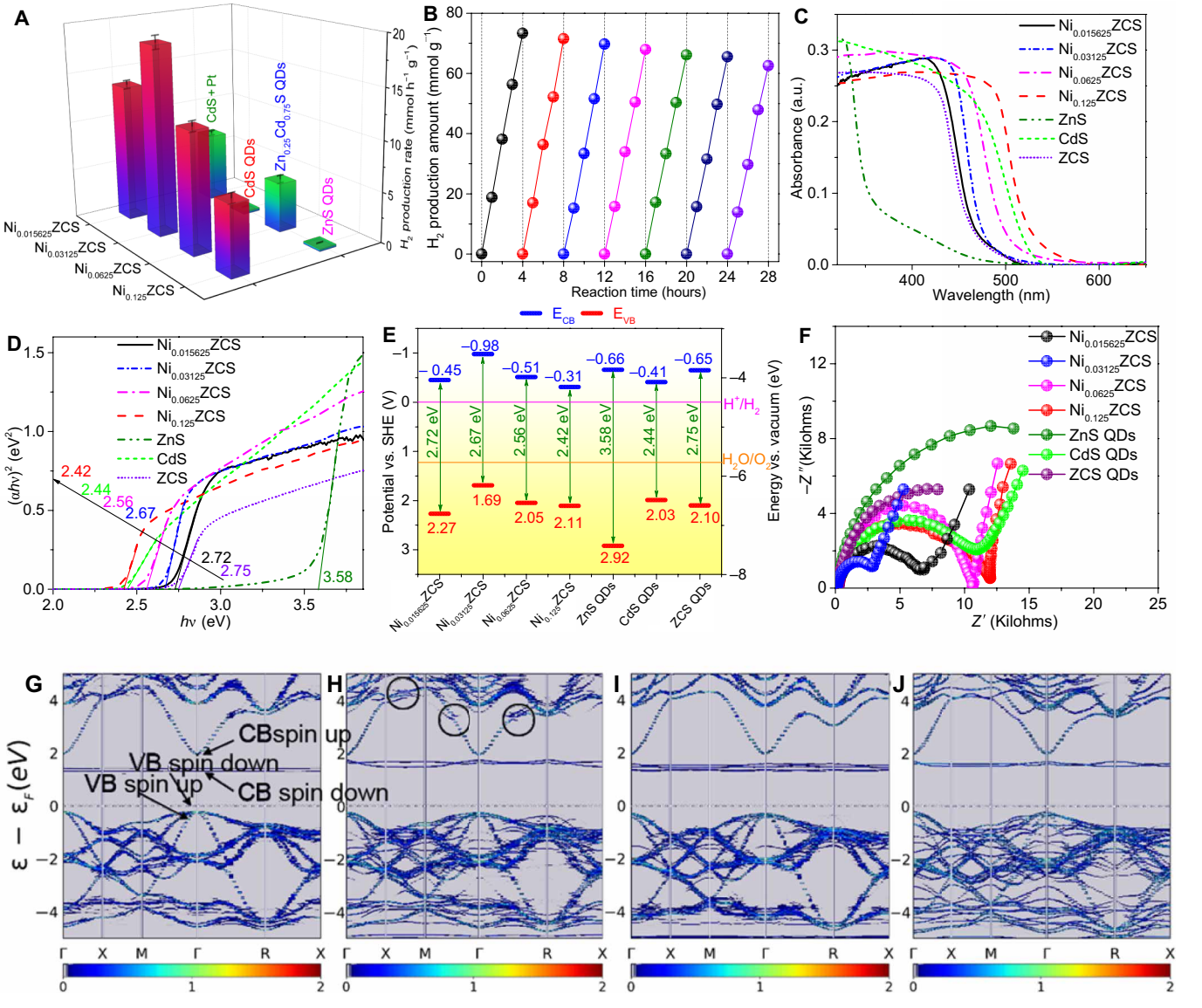

Fig. 4. Photocatalytic performance and spectroscopy/(photo)electrochemical characterization. (**A**) A comparison of the photocatalytic H_2 production activities of Ni_xZCS (x = 0.015625, 0.03125, 0.0625, and 0.125) QDs, Pt-CdS QDs, CdS QDs, ZCS QDs, and ZnS QDs. The error bars denote SD. (**B**) Time course of photocatalytic H_2 production over $Ni_{0.03125}$ZCS; every 4 hours, the reaction system was purged with Ar for 30 min to remove H_2. (**C**) Ultraviolet-visible (UV-vis) diffuse reflectance spectra of Ni_xZCS (x = 0.015625, 0.03125, 0.0625, and 0.125) QDs, CdS QDs, ZCS QDs, and ZnS QDs. (**D**) The plots of transformed Kubelka-Munk function of the Ni_xZCS (x = 0.015625, 0.03125, 0.0625, and 0.125) QDs, CdS QDs, ZCS QDs, and ZnS QDs. (**E**) Electronic band structures of Ni_xZCS (x = 0.015625, 0.03125, 0.0625, and 0.125) QDs, Pt-CdS QDs, CdS QDs, ZCS QDs, and ZnS QDs. (**F**) EIS Nyquist plots of Ni_xZCS (x = 0.015625, 0.03125, 0.0625, and 0.125) QDs, CdS QDs, ZCS QDs, and ZnS QDs electrodes measured under the open-circuit potential of electrodes with visible-light irradiation. (**G** to **J**) Unfolded band structure of the supercell for bulk Ni_xZCS (x = 0.015625, 0.03125, 0.0625, and 0.125) crystals, demonstrating the direct bandgap. The Fermi level moves to 0, as indicated by the dashed lines.

calculated based on the generalized gradient approximation (GGA) exchange-correlation function, due to the underestimation by the GGA function (*34*). To gain insights into the charge separation and transfer mechanism induced by the Ni dispersion, the unfolded band structures were calculated (Fig. 4, G to J). For the bulk Ni_xZCS crystals, both the CB minimum (CBM) and VB maximum (VBM) are found to be located at the Γ point of the Brillouin zone (BZ; fig. S8, A to C) with the direct bandgap transition. Along with the Ni doping level increase, the CB edge was reduced gradually. This indicates that Ni doping induced considerable energetic elevation of the CBM, which could contribute to narrowing the overall energy gap in the doped materials (2.49, 2.43, 2.38, and 2.31 eV for $Ni_{0.015625}$ZCS, $Ni_{0.03125}$ZCS, $Ni_{0.0625}$ZCS, and $Ni_{0.125}$ZCS, respectively), which is consistent with the Kubelka-Munk (K-M) results and the UV-vis spectra (Ni_xZCS QDs have gradually decreasing bandgaps of 2.72, 2.67, 2.56, and 2.42 eV, respectively, Fig. 4D). The narrowed bandgap with Ni dopant has been reported by Thambidurai *et al.* (*35*), Zhang *et al.* (*12*), and Wu *et al.* (*36*). The strong Ni spin polarizations in Ni_xZCS become more notable with increased Ni concentration. Moreover, besides the Ni spin-down orbit-introduced energy level between VBM and CBM, several flat bands related to the electron localization around the Ni and Zn region can be found, accompanied by breaking the branch of the bonds (as circled in Fig. 4, G to J). The charge densities of CBM and VBM states (spin up and down) at Γ indicate that the dominant orbit components are Ni t_{2g} ($3d_{xy}$, $3d_{xz}$, or $3d_{yz}$) and S $2p_z$ for CBM, while S $2p_x$, $2p_y$, or $2p_z$ together with a minority of Ni t_{2g} contributed to the VBM (fig. S8, D to V). For the (110) facets, CBM is also ascribed to the Ni spin-down 3d t_{2g} (d_{xy}, d_{xz}, or d_{yz}) state with slightly decreased bandgap (E_g), whereas the (111) facets demonstrated the increased bandgap along with the increased Ni in Ni_xZCS host crystals (fig. S8, w_1 to w_4 and x_1 to x_4). The Fermi level (E_f) and work function (Φ) are E_f = −2.99, −2.94, −2.88, and − 2.83 eV and Φ = 5.96, 5.94, 5. 92, and 5.8 versus vacuum level for the (110) facets of Ni_xZCS (x = 0.015625, 0.03125, 0.0625, and 0.125), respectively. The values are −3.40, −3.33, −3.37, and − 3.62 eV (E_f) and 4.6, 4.48, 4.56, and 4.68 (Φ) for the (111) facets, respectively. Accordingly, Fig. 5A shows the band edge (VBM and CBM) alignment of the (110) and (111) facets of Ni_xZCS, demonstrating the typical type II (staggered) heterojunctions. Electrons in the (111) crystal planes with the higher Fermi levels tend to flow to the (110) crystal planes to flatten the Fermi levels. Therefore, the (110) facets here had considerable excess negative charges, whereas the (111) facets were electropositive to some extent. The adjustment of Fermi levels brought in the rearrangement of overall band structures (Fig. 5B), in which, to accommodate the flattened Fermi levels, both CBM and VBM of (110) parallelly shifted up, whereas CBM and VBM of (111) synchronously descended. Such rearranged band structures are consistent with the experimental Mott-Schottky plots and VB spectra (Fig. 4E and fig. S9, A to D). The CBMs of Ni_xZCS QDs were measured to be at −0.45, −0.98, −0.51, and −0.31 V versus the standard hydrogen electrode (SHE) for Ni_xZCS (x = 0.015625, 0.03125, 0.0625, and 0.125), respectively (Fig. 4E). The flattening of Fermi levels and electron flow could generate the BIEF between the (110) and (111) facets, forming a charge disequilibrium in the depth direction perpendicular to the interface (Fig. 5B). Furthermore, when evaluating the energy levels of the (110) and (111) facets of the same Ni_xZCS (Fig. 5B), the difference in energy of the VB and CB between the (110) and (111) facets can be distinct. It suggests that the electron transfer from the (110) and (111) facets is feasible thermodynamically, leading to the accumulation of electrons on the (111) facets. Such spatial charge separation between the (110) and (111) facets is feasible due to their different energy levels, which is responsible for the formation of reduction and oxidation facets. Meanwhile, the opposite BIEF direction toward the electron flow markedly accelerates the migration of photoexcited electrons from the (110) to the (111) facets, whereas the immobilized positive holes near the (110)/(111) interface remain on the (110) facets because of the high repulsive force from the BIEF. It is worth noting that such synergetic effects of various coexposed facets in one crystal and balanced ratio of different exposed facets is crucial for the photocatalytic efficiency. The band bending of each facet of Ni_xZCS (x = 0.015625, 0.03125, 0.0625, and 0.125) and the BIEF are distinct owing to their different surface electronic structures, which is another factor affecting the spatial charge separation. The downward bent (110) VB and the upward bent (111) VB generate discontinuities at their interface, forming a barrier for holes to transfer from the (110) to the (111) facets, in spite of which the location of the (111) VBM is more favorable for hole migration. Thus, because of such favorable band structure and BIEF, photoexcited electrons could smoothly transfer from (110) to (111), whereas the holes stay within their respective facets. Such separated pathways could drastically increase the photoexcited charge carrier separation efficiency (*37*) as demonstrated by Fig. 5C. Moreover, owing to the different barrier height, the large offsets of VB and CB between the (110) and the (111) facets could enhance the driving force for the separation of photoexcited electrons and holes (*38*). $Ni_{0.03125}$ZCS presented the largest ΔE_{CBM} (~0.54 eV), which is consistent with the most negative CBM as measured (Fig. 4E), indicating its strongest charge separation and hydrogen reduction capability. The ΔE_{CBM} decreased to 0.35 eV for $Ni_{0.0625}$ZCS. For $Ni_{0.125}$ZCS, owing to the increased E_g of the (111) facets, both the CB and VB of the (110)/(111) interface generate discontinuities, impeding the transfer of both photoexcited electrons from (111) to (110) facets and holes from (110) to (111) facets. Such limited surface heterojunction cannot drive the charge pair separation. The charge carrier separation efficiency was validated by photoluminescence (PL) spectra (fig. S9E) and transient photocurrent (TPC) response. The strong recombination of electrons at the CBM and the holes at VBM produced a broad peak centered at ~533 nm. $Ni_{0.03125}$ZCS QDs exhibit the lowest PL peak intensity, implying the most efficient charge carriers separation and transfer. The PL intensity of other QDs follow the sequence $Ni_{0.015625}$ZCS QDs < $Ni_{0.0625}$ZCS QDs < $Ni_{0.125}$ZCS QDs < ZCS QDs < CdS QDs < ZnS QDs, suggesting a suppressed photoexcited charge carrier recombination. The TPC densities show the same trend (fig. S9f). The photocurrent response for $Ni_{0.03125}$ZCS QDs gives the highest current density under intermittent visible-light illumination (fig. S9g), followed by $Ni_{0.015625}$ZCS QDs, $Ni_{0.0625}$ZCS QDs, $Ni_{0.125}$ZCS QDs, ZCS, CdS QDs, and ZnS QDs. The surface charge-transfer efficiencies were measured by electrochemical impedance spectroscopy (EIS) (Fig. 4F). The semicircle diameters follow the sequence $Ni_{0.03125}$ZCS QDs > $Ni_{0.015625}$ZCS QDs > $Ni_{0.0625}$ZCS QDs > $Ni_{0.125}$ZCS QDs, also indicating much lower interfacial charge-transfer resistance of $Ni_{0.03125}$ZCS QDs (table S6). All these results confirmed that doped ZCS QDs, especially the $Ni_{0.03125}$ZCS QDs, show good interfacial charge carrier transfer and superior charge carrier separation ability.

The LDOS shows that the much tighter and sharper 3d t_{2g} and e_g orbits of Ni in (110) facets have greater localization state than the

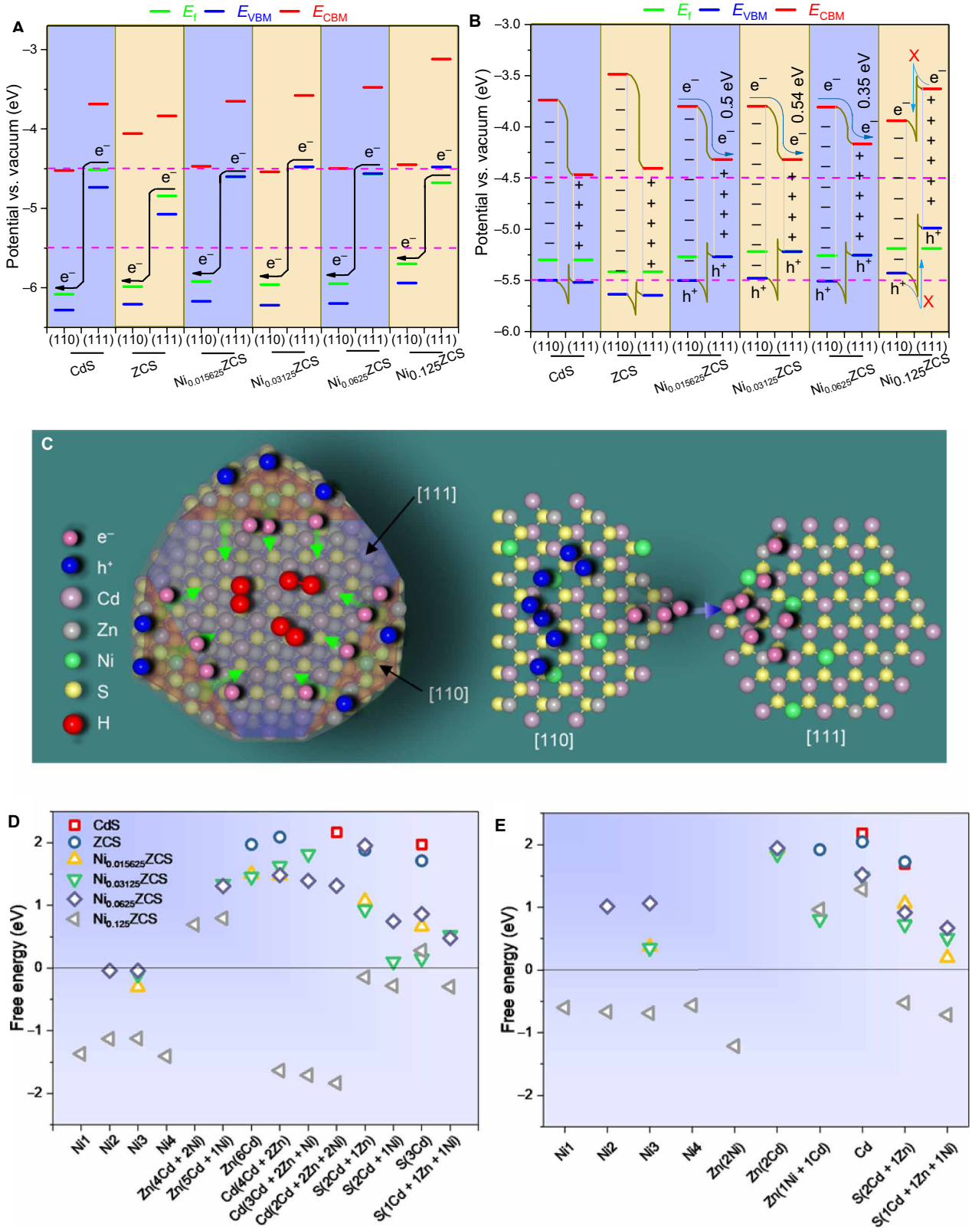

Fig. 5. DFT calculation studies. (**A**) The calculated electronic band structures of (110) and (111) facets of Ni_xZCS ($x = 0.015625$, 0.03125, 0.0625, and 0.125), CdS, and ZCS. (**B**) The band structure layouts after accommodation of Fermi levels. (**C**) Schematic diagram of the BIEF at the interface formed by (110) and (111) facets, contributing a surface heterojunction to reduce the electron-hole recombination. (**D** and **E**) Free energy of the hydrogen (H*) adsorption on different Ni, Zn, Cd, and S sites on the surface of (111) (D) and (110) (E) crystal planes of the Ni_xZCS ($x = 0.015625$, 0.03125, 0.0625, and 0.125), CdS, and ZCS.

ones in (111) facets (fig. S10, A to H). More Ni 3d electrons in (111) facets, especially the spin-down electrons, are involved in the hybridization with the S s and p orbits owing to their flatter surface feature, leading to the shift of weight in intensity from the CB to the VBM. Thus, it results in higher charge density and partial charge of Ni in (111) than in (110) at the VBM (fig. S10, I to L). The unpaired spin-up electron of monovalent Ni(I) in (111) facets was identified to occupy the high–energy level $3d_{x^2-y^2}$ and $3d_{z^2}$ orbits, which could provide high reactivity toward the catalytic reactions (*9*), whereas the two unpaired electrons of Ni in (110) facets mainly occupy the $3d_{xy}$ and $3d_{xz}$ orbits. Moreover, the Ni d-bond center of the (111) facets is much closer to the Fermi level (fig. S10, M and N), exhibiting a strong hydrogen adsorption ability via the higher antibonding states together with a proton from the electrolyte (*39*). The H*, HO*, and O* species adsorption on different Ni, Zn, Cd, and S sites of the cleavage (110) and (111) surface of Ni_xZCS was studied to verify their HER activity. The corresponding free energy change ΔG_H*, ΔG_{OH}*, and ΔG_O* are shown in Fig. 5 (D and E) and fig. S10. For both (111) and (110) surfaces, the anion sites (S), supplying electrons, are favored for the H* adsorption (showing the low $|\Delta G_H^*|$, Fig. 5, D and E). S sites on the (111) surface show the more favorable activities for the H* adsorption than the ones on the (110) surface. As shown by the charge density difference figures (fig. S11, A to H), the S on the (111) surface coplanarly coordinate with Ni, Zn, and Cd ions, making the H* perpendicularly absorbed. This benefits the electron transfer from S to H* with appropriate bonding energy. Meanwhile, M metals from the lower layer contribute electrons to avoid too strong bonding energy between S and H*. As compared, H* forms the slanting angle toward S sites on the (110) surfaces (fig. S11, I to P), showing higher free energy than that on the (111) surfaces (Fig. 5, D and E). It is ascribed to the extra charge contribution from M sites bonding with S, owing to their shorter distance.

These results indicate that the (111) surface is more favorable for the HER than the (110) surface. Moreover, because of the BIEF established by the surface heterojunction and rearranged band levels between the (110)/(111) interface, photoexcited electrons transfer from (110) to (111), further enhancing the catalytic activity of the (111) surface for HER. Thus, with less (111) facets, $Ni_{0.0625}ZCS$ and $Ni_{0.125}ZCS$ have a decreased HER ability. Owing to the occurrence of a single e_g lone electron of the monovalent Ni(I) d9 structure on the (111) surfaces, Ni sites on (111) surfaces of $Ni_{0.015625}ZCS$, $Ni_{0.03125}ZCS$, and $Ni_{0.0625}ZCS$ also show the low $|\Delta G_H^*|$ values (0.30, 0.11, and 0.04 eV, respectively, Fig. 5D). Nevertheless, very strong adsorption energy bonds H* tightly on the Ni site in the $Ni_{0.125}ZCS$ (111) surface, contrary to HER properties (fig. S11, Q, S, U, and W). Because of more unpaired electrons on Ni d8 of the (110) surface, both Ni and S sites on the (110) surface contributed large charge density to H* (fig. S11, R, T, V, and X). As shown in fig. S11 (y_1 and y_2), HO* prefers to be adsorbed on cation sites for both (110) and (111) surfaces. In particular, the $Ni_{0.03125}ZCS$ demonstrated the low $|\Delta G_{OH}^*|$ on all M sites of (111) and (110) surfaces [~0.36, ~0.42, and ~0.40 eV for Ni, Zn, and Cd on the (111) surface and 0.75, ~0.43, and 0.80 eV for Ni, Zn, and Cd on the (110) surface, respectively]. The (110) surfaces show that the lowest $|\Delta G_{OH}^*|$ on S sites coordinated with Cd, Zn, and Ni, which is beneficial for oxygen evolution. O* also prefers the anion and Ni sites (fig. S11, z_1 and z_2), which can be ascribed to the low magnetic moment of O* on these sites because of the paired occurrence of lone electrons between O* and S and Ni sites in the geometry. Among Ni_xZCS QDs, $Ni_{0.0325}ZCS$ QDs show the lowest $|\Delta G_O^*|$ on the active sites of both (110) facets, indicating its OER activity. Obviously, the BIEF established by surface heterojunction and rearranged band levels in the same phase greatly facilitate the charge carriers' separation and transfer in the reverse direction, which enhances the (111) and (110) surfaces for HER and OER, respectively.

Electronic structures

The bonding nature of H_2O on the Ni, Zn, and Cd species of $Ni_{0.03125}ZCS$ (110) and (111) facets was further investigated by the projected densities of states (PDOS) (Fig. 6 and fig. S12). For both (110) and (111) facets, the energy levels of Ni d orbits and H_2O $1b_1$ orbits are matched, leading to partial occupation of the formed d-1b1 orbits (Fig. 6, A and C). The fragment orbit analysis provides more details of the interaction between Ni and H_2O (Fig. 6, B and D). It shows that the spin-up Ni d_{xz} orbit on the (110) facet (Fig. 6B) and the spin-down Ni d_{z^2} orbit on the (111) facet (Fig. 6D) can provide large exchange stabilization energy for the 1b1 orbits of H_2O, forcing $*H_2O$ to be of radical nature for hydrogenation. The partial $1b_1$ orbit of H_2O was enhanced above the Fermi level, leading to the antibonding orbit and lowering the O—H bonding energy level, which further weakens the H—O bond. Therefore, the more interaction and lower occupation of the $1b_1$ orbit in H_2O show a lower H—O bond order, which is responsible for the lower dissociation barrier than that of $*H_2O$. The crystal orbit overlap population (COOP) analyses (Fig. 6, E and F) also show that under the Fermi level, the Ni d_{z^2} on the (111) facet presents more overlap population with both O and H to form the bonding feature. Meanwhile, H—O forms the antibonding feature, indicating the radical nature for hydrogenation. The d_{xz} orbit of Ni on the (110) facet only generated the bonding feature with O. The H forms the antibonding with Ni d_{xz} and H—O still bonds tightly. Obviously, the flatter crystal plane feature of the (111) facet more easily transfers electrons from the Ni d_{z^2} orbit to the H_2O $1b_1$ orbit, weakening the H—O bond, lowering the bond order in H_2O, and facilitating the hydrogenation process. For both Zn and Cd, the d orbits match the $1b_2$ orbit of H_2O with much lower energy level (fig. S12, A to D), which could not contribute a large amount of electron transfer from Zn and Cd to H_2O (fig. S12, E, F, H, and I). The corresponding COOP analyses also revealed their limited bonding feature with H and O (fig. S12, G and J). Therefore, the Ni dispersion in Ni_xZCS QDs plays a crucial role in HER.

The triethanolamine (TEOA) interaction with the $Ni_{0.03125}ZCS$ (110) and (111) facets was also studied to identify the H_2 evolution from TEOA (fig. S13). As shown by the charge density difference plots of TEOA adsorption on $Ni_{0.03125}ZCS$ (110) and (111) (fig. S13, B and C), both the (110) and (111) facets demonstrate strong charge transfer between Ni, Cd, and Zn sites with different H sites of TEOA (H_O, Hc_1, and Hc_2, which coordinated with O, C_1, and C_2 of TEOA, respectively, as shown in fig. S13A). Besides the Ni, Cd, and Zn sites, their coplanarly coordinated S sites on (111) facets or their adjacent and in the same plane S sites on (110) facets also transfer the charge to the TEOA. Such interactions can be verified by the PDOS of Ni, Cd, Zn, and S on $Ni_{0.03125}ZCS$ (110) and (111) facets together with different H sites of TEOA (H_O, Hc_1, and Hc_2), as shown in fig. S13 (D, E, H, and I). For the bare TEOA, the Hc_2 shows the PDOS near the Fermi level, followed by Hc_1 and H_O, respectively (fig. S13D), indicating their dehydrogenation ability from TEOA. For both (110) and (111) facets, the energy levels of Ni orbits and

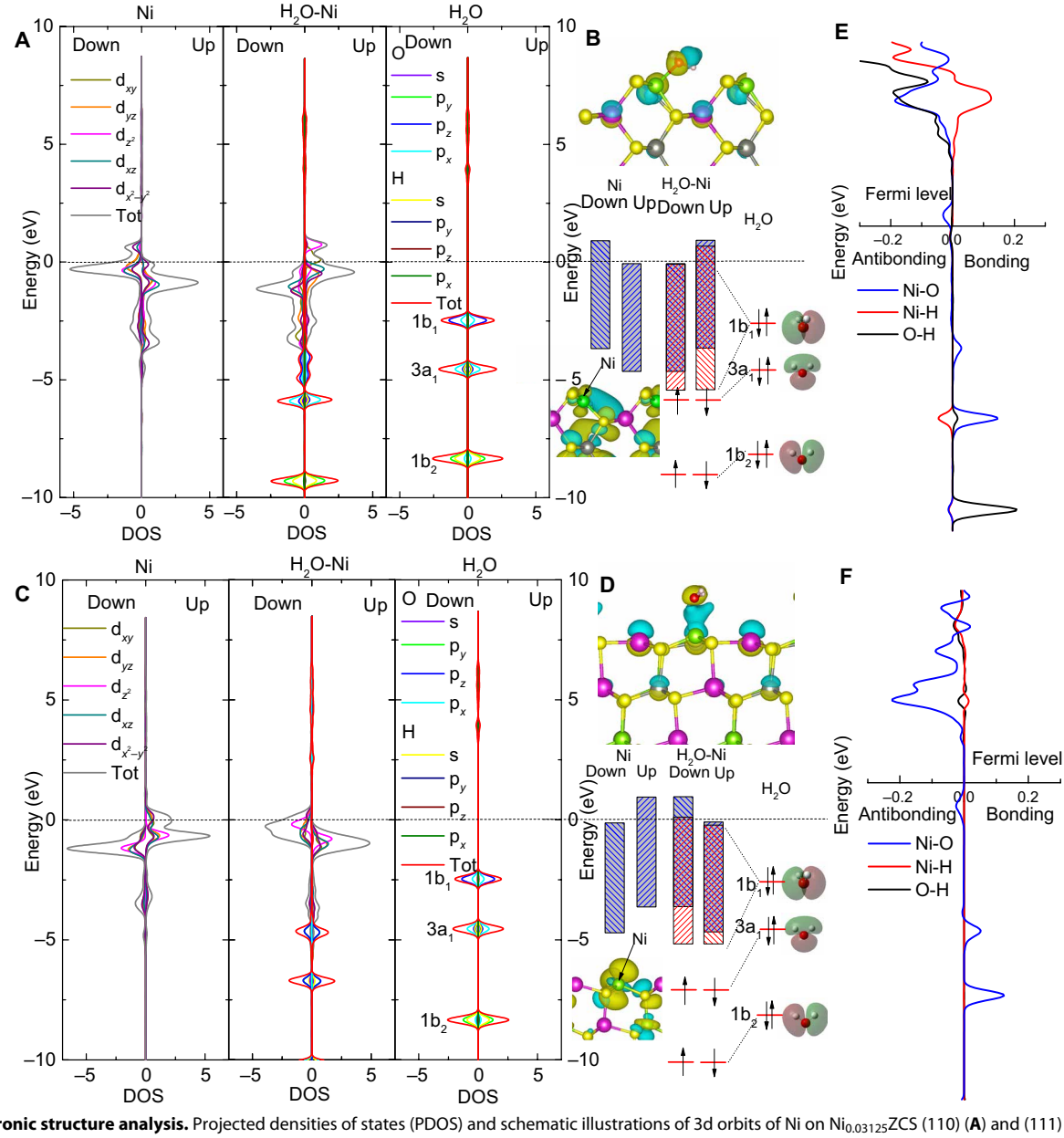

Fig. 6. Electronic structure analysis. Projected densities of states (PDOS) and schematic illustrations of 3d orbits of Ni on $Ni_{0.03125}$ZCS (110) (**A**) and (111) (**C**), 1s, 2s, and 2p orbits of the H_2O molecule, and their interaction within H_2O-Ni configuration, Tot represents the sum of PDOS of each orbits. (**B** and **D**) PDOS and schematic illustrations for the H_2O-Ni on $Ni_{0.03125}$ZCS (110) (B) and (111) (D) case and charge density differences of H_2O adsorption on $Ni_{0.03125}$ZCS (110) and (111) (cyan stands for holes and yellow stands for electrons). (B) and (D) also demonstrated the major interactions and energy levels of the molecular orbits of H_2O on Ni of (110) and (111) facets with correlation to the orbits from Ni and H_2O fragments. (**E** and **F**) Crystal orbit overlap population (COOP) for H_2O on Cd and Zn of $Ni_{0.03125}$ZCS (110) (A) and (111) (B) models. The balls in green, gray, purple, yellow, red, and white colors represent the Ni, Zn, Cd, S, O, and H atoms, respectively.

Hc_1 and Hc_2 orbits are matched, leading to partial occupation of the formed Ni-Hc_2 and Ni-Hc_1orbits (fig. S13, D and E). Their corresponding COOP plots (fig. S13, F and G) also show that under the Fermi level, the Ni on both (110) and (111) facets presents overlap population with Hc_1 and Hc_2 to form the bonding feature. In particular, the Ni on (110) facets shows more overlap population with Hc_1 than the one on (111) facets, which could be ascribed to the two unpaired electrons of Ni on (110) facets, contributing to more interaction with the H than that on (111) facets. Relative to Cd, Zn on (110) facets demonstrates the bonding feature with Hc_1 (fig. S13F), which could be ascribed to more matched energy levels of Zn orbits and Hc_1 on (110) facets (fig. S13D), while both Zn and Cd on (111) facets could bond with Hc_1 and Hc_2 (fig. S13G) due to their lower PDOS energy levels, which matches the Hc_2 and Hc_1 energy levels (fig. S13E). Meanwhile, because of the strong charge transfer between TEOA and coplanarly coordinated S sites with metals on (111) facets or in the same plane adjacent S sites to metals on (110) facets (fig. S13, B and C, S_{Ni}, S_{Cd}, and S_{Zn} represent the S coordinated with or adjacent to Ni, Cd, and Zn, respectively), the S PDOS of (110) and (111) facets together with H_O, Hc_1, and Hc_2 were also

calculated (fig. S13, H and I). It can be seen that the PDOS of S are more overlapped with H from TEOA. Therefore, they form the bonding feature with H (fig. S13, J and K). In particular, the S adjacent to Ni on the (110) facets generates the strong bonding feature with H_O, Hc_1, and Hc_2, while S adjacent to Cd and Zn bonds well with H_O than with Hc_1 and Hc_2. For the coplanarly coordinated S sites on (111) facets, their PDOS are pushed down, showing more matched energy levels with Hc_1. Therefore, it results in more bonding features between S and Hc_1 as shown in their corresponding COOP analyses (fig. S13K). Obviously, the flatter crystal plane feature of the (111) facets more easily transfer electrons to the TEOA orbit, weakening the Hc_1—C_1 bond, lowering the bond order in TEOA, and facilitating the hydrogenation process. Furthermore, we also calculated the adsorption energy of TEOA on $Ni_{0.03125}$ZCS (110) and (111) facets. The results show that the adsorption of TEOA on (111) facets is much stronger than that on (110) facets (with the adsorption energy of −0.6 eV versus −0.2 eV), and the O—H bonds within TEOA are elongated more evidently on the (111) surface (0.99 Å) compared to that on (110) (0.97 Å). Therefore, the photogenerated holes on (111) facets can be more efficiently consumed by TEOA than on (110). The sequential oxidation of TEOA on (111) facets, induced by photogenerated holes, could produce acetaldehyde and diethanolamine on the basis of the reaction $NR_3 \rightarrow CH_3CHO + HNR_2$, (R = C_2H_4OH, fig. S14A) (*40*–*42*). The COOP between N with C_2 of TEOA absorbed on (111) facets demonstrated a much weaker bonding feature compared with the bare TEOA and TEOA absorbed on (110) facets (fig. S14B). Oxidation of acetaldehyde and diethanolamine could produce hydrogen and contribute to the H_2 evolution. Therefore, the COOP between H sites on acetaldehyde and diethanolamine and Ni, Cd, and Zn on (111) facets were further calculated. It can be seen that there is no readily bonding feature between H sites on acetaldehyde with Ni, Cd, and Zn (fig. S14C) and H sites on diethanolamine with Zn (fig. S14D), while H_N (H coordinated with N of diethanolamine), Hc_2, and Hc_1 form the bonding feature with Cd and Ni (fig. S14, E and F). Here, the systematic evaluation of electronic structures of the Ni_xZCS QDs actualizes the synergetic integration of photocatalytic constituents into a functional heterostructure to optimize the photocatalytic activity for HER.

Conclusions

In summary, we demonstrate a strategy to optimize the atomically dispersed Ni within the zincblende Ni_xZCS QDs to maximize their efficient and durable photocatalytic performances for water splitting driven by sunlight. The fine-tuned atomically Ni-dispersed Ni_xZCS QDs achieved an ultrahigh photocatalytic H_2 production activity of 18.87 mmol $hour^{-1}$ g^{-1}. The combination of the experimental investigation and DFT calculations revealed the mechanisms of achieving such high photocatalytic performances. These include (i) the favorable surface engineering of the as-prepared $Ni_{0.03125}$ZCS QDs with the highly active sites of monovalent Ni(I) on the (111) facets, (ii) the surface heterojunctions between the anisotropic (110)/(111) interface to reinforce the carrier separation owing to the BIEF, and (iii) appropriate surface H_2 adsorption thermodynamics. This work demonstrates a synergistic regulation of the physicochemical properties of QDs at the atomic level toward high-efficiency photocatalytic H_2 production. Therefore, the reported approach could provide an effective avenue for optimizing the accurate amount of the introduced heterogeneous elements into the catalysts to simultaneously boost the intrinsic activity, site density, electrical transport, and stability.

MATERIALS AND METHODS

Synthesis of the Ni_xZCS (x = 0.015625, 0.03125, 0.0625, and 0.125) QDs

The synthetic procedures for Ni_xZCS (x = 0.015625, 0.03125, 0.0625, and 0.125) QDs are as follows: the OLA (≥98%, Sigma-Aldrich) was firstly degassed under vacuum at about 100°C for 30 min. After cooling to room temperature, the Ni, Zn, and Cd chlorides (98%, Sigma-Aldrich) and TAA (≥99%, Sigma-Aldrich) were stoichiometrically dispersed in 5 ml of OLA, respectively. Then, Ar was bubbled through the solution for 30 min and followed by heating to certain temperatures (for Ni, Zn, Cd, and S, the temperature are 200°, 230°, 160°, and 90°C, respectively) to form a homogeneous and clear solution. After that, the resulting solutions were injected into a three-necked flask and the mixture was flash-heated to 220°C and aged at that temperature for 30 min, resulting in a colloidal solution. Ethanol (≥99%, Sigma-Aldrich), methanol (≥99.9%, Sigma-Aldrich), and chloroform (≥99.5%, Sigma-Aldrich) (2:1:4 in volume ratio) were added to precipitate the QDs. The precipitate was retrieved by centrifugation and was then redispersed in cyclohexane and subjected to another three rounds of purification. The obtained powders were redispersed easily in nonpolar solvents such as hexane, toluene, and cyclohexane.

Structural and physical characterization

The crystal structures and phases of the Ni_xZCS (x = 0.015625, 0.03125, 0.0625, and 0.125) QDs were examined by powder XRD (Bruker D8 Discover XRD) using Cu K_α radiation. The morphology was characterized by FESEM (Zeiss Supra 55VP), and the details of the crystal structure of the Ni_xZCS (x = 0.015625, 0.03125, 0.0625, and 0.125) QDs were identified by TEM and HRTEM (JEM-2011, JEOL). The images were collected by a Gatan charge-coupled device (CCD) camera in a digital format. Atomic resolved HRTEM images and EDS mapping were obtained by HAADF-STEM (JEM-ARM200F, JEOL) at an accelerating voltage of 200 keV and the Oxford EDS system. The energy resolution at the zero-loss peak was 0.3 eV. The spectra were acquired from thin regions of ~20 to 100 nm. Care was taken to ensure that samples were not damaged by the electron beam by applying liquid-nitrogen cooling. All operation and postprocessing of the HAADF-STEM images were conducted by Digital Micrograph software. ICP-MS (Agilent 7500 Series) was used to quantify the elemental composition. EELS spectra were acquired with a Gatan 666 parallel EELS spectrometer attached to the JEM-ARM200F (JEOL) operated at an accelerating voltage of 200 keV. The energy resolution at the zero-loss peak was 0.3 eV. The spectra were acquired from thin regions of ~20 to 100 nm. Care was taken to ensure that samples were not damaged by the electron beam by liquid-nitrogen cooling. All operation and postprocessing of the EELS spectra were conducted by Digital Micrograph software. The white-line ratio on the EELS profile was calculated from the area under Ni L-edge each peak by eliminating the background intensity via a method suggested by Pearson *et al.* (*43*). XPS measurements were carried out on a Kratos XSAM-800 spectrometer with an Mg K_a radiation source. UV-vis diffuse reflectance spectra were collected for the dry pressed disk samples with a UV-vis spectrophotometer (LAMBDA 950 UV-vis/near infrared spectrometer, PerkinElmer)

using $BaSO_4$ as the reflectance standard at room temperature. Steady-state PL spectra were tested on a Varian Cary Eclipse fluorescence spectrometer at room temperature. The optical images were collected with a Canon EOS 660D camera. Here, the bandgaps of the samples were calculated by the K-M method on the basis of the UV-vis diffuse absorption spectra by the following equation (*44*)

$$\alpha h\nu = A(h\nu - E_g)^{1/2}$$

where α, $h\nu$, and E_g are the absorption coefficient, the photon energy, and the direct bandgap, respectively; A is a constant.

XAFS measurements

The XAFS spectra were collected at the 1W1B station of the Beijing Synchrotron Radiation Facility (operated at 2.5 GeV with a maximum current of 250 mA, Pt L_3-edge). XAFS measurements at the Ni K-edge were performed in fluorescence mode using a Lytle detector. All samples were pelletized as disks of 13-mm diameter with 1-mm thickness using graphite powder as a binder. All spectra were collected in ambient conditions.

EXAFS analysis

The acquired EXAFS data were processed by postedge background subtraction from the overall absorption and normalizing with respect to the edge-jump step using the ATHENA module implemented in the IFEFFIT (*45*). Then, $\chi(k)$ data in the k-space ranging from 2.6 to 12.6 $Å^{-1}$ were Fourier-transformed to real (R) space using Hanning windows (dk = 1.0 $Å^{-1}$) to separate the EXAFS contributions from different coordination shells. The quantitative information can be obtained by the least-squares curve fitting in the R space with an FT k-space range of 3 to 11.26 $Å^{-1}$. The backscattering amplitude $F(k)$ and phase shift $\Phi(k)$ were calculated using FEFF8.0 code (*46*). First-principles scattering amplitudes and phase shifts for the photoelectron path of Ni-S and Ni-Cd(Zn) were calculated using Hartree-Fock "muffintin" potential accounting for the screened 1s hole of the absorbing Ni atom (*47*). To examine the effect of the second and third shells on the determined local structure of the absorbing atom, three series of fits were performed in R space including one, two, and three coordination shells of Ni.

Ni K-edge XANES spectra simulation within DFT framework

The projected p state density of electronic states (pDOS) provided by DFT calculation of NiS_x (x = 6, 4, and 3) complexes were compared with KXANES spectra since the K-absorption cross section σ(ω) (ω is the energy of x-ray photons) reflects mainly the energy structure of the empty p states on the absorbing Ni atom according to the dipole selection rule. To validate the application of the DFT method to the structural modeling of NiS_x (x = 6, 4, and 3) complexes, their corresponding molecular orbital energy levels were analyzed. The dependence of σ(ω) and pDOS is established according to the Fermi's Golden rule in the dipole and one electron approximations by the expression: $\sigma(\omega) = C|\langle\Psi_f|\nabla|\Psi_{1s}\rangle|^2\rho(\hbar\omega + E_{1s})$, where C is the constant coefficient, and Ψ_{1s} and Ψ_f are the wave functions of the 1s state of Ni atom and the final p symmetrical state with energy $E_f = \hbar\omega + E_{1s}$, respectively. $\rho(E_f)$ is the pDOS at Ni atom, and ∇ is the operator of dipole transition. It can be seen that the fine structure of $\rho(E_f)$ or KXANES is determined mainly by the energy dependence of pDOS on the absorbing atom in assuming of the smooth energy dependence of the matrix element.

Electrochemical measurement

The surface charge-transfer efficiencies were investigated by the EIS measurements, which were carried out on a CHI 660C electrochemistry workstation with a standard three-electrode system using the synthesized Ni_xZCS (x = 0.015625, 0.03125, 0.0625, and 0.125) QDs coated on F-doped SnO_2-coated glass (FTO glass) as the working electrodes, and a Pt wire and Ag/AgCl (saturated KCl) as the counter electrode and reference electrode, respectively. The working electrodes were synthesized as follows: 10 mg of the sample and 1 mg of naphthol (99%, as the binder, Sigma-Aldrich) were dispersed in 10 ml of ethanol. After sonification for several minutes to get the uniformly distributed precipitation solution, 1 ml of solution was dropped onto a 1 cm by 1.5 cm FTO glass electrode via a pipette. The obtained electrode was dried in an oven for 0.5 hours. All working electrodes studied were kept at a similar mass loading of 1 mg. For the TPC density measurement, Na_2S and Na_2SO_3 within the electrolyte worked as hole scavengers rapidly capturing the photoinduced holes on the surface of QDs, which can eliminate the surface charge recombination of QDs. Therefore, the collected TPC density reflects the charge separation efficiency in the bulk of the QD samples. The polarization curves were recorded in the abovementioned three-electrode system and the bias sweep range was from −0.4 to −0.9 V versus SHE with a step size of 0.005 V. The Mott-Schottky plots were also measured by the same three-electrode system using the synthesized Ni_xZCS (x = 0.015625, 0.03125, 0.0625, and 0.125) QDs coated on FTO glass as the working electrodes without naphthol binder over an AC frequency of 1200 Hz in 0.5 M Na_2SO_4 aqueous solution. A 300-W xenon light with an UV-cutoff filter (λ ≥ 420 nm) was applied as the light source.

The experimental measurements of photocatalysis

The H_2 evolution was characterized in a 50-ml Pyrex flask (sealed with silicone rubber septa) at ambient temperature and atmospheric pressure. Before the experiment, all glassware was rinsed carefully with deionized water. A Xe arc lamp (300 W) with a UV-cutoff filter (λ ≥ 420 nm) was applied as a light source to trigger the photocatalytic reaction. The focused intensity on the flask was ca. 80 mW cm^{-2}. In the typical photocatalytic measurement process, 10 mg of photocatalyst was suspended with constant stirring in a mixed solution of TEOA and water (20 volume %, as a sacrificial reagent). Before irradiation, the suspension was sonicated and bubbled with argon gas for half an hour to remove residual and dissolved air and keep the reaction system under anaerobic conditions. During the irradiation process, 0.2 ml of gas was sampled intermittently through the septum, and the H_2 content was analyzed by a gas chromatograph (Clarus 480, PerkinElmer, TCD with Ar as a carrier gas and a 5-Å molecular sieve column). For comparison, the CdS QDs, ZnS QDs, and ZCS QDs and the Pt-CdS QDs were also measured for H_2 evolution. For loading the cocatalysts, 1 wt % Pt was deposited onto the surface of photocatalysts by the in situ photodeposition approach using H_2PtCl_6 (≥37.5%, Sigma-Aldrich) under Xe arc lamp (300 W) irradiation for 40 min.

Theoretical calculations

DFT calculations were performed using the Vienna Ab initio Simulation Package (*48*) on the basis of the GGA with the Perdew-Burke-Ernzerhof function as the exchange-correlation energy function. For the bulk crystals of Ni_xZCS (x = 0.03125, 0.0625, and 0.125), 2 × 2 × 2 unit cells [relative to the face-centered cubic (fcc) zincblende

CdS unit cell, 4 Cd and 4 S atoms, respectively] with 64 atoms (with 1, 2, and 4 Ni atom substitution, respectively) were used for the crystal structure and electronic structure calculations. For the $Ni_{0.03125}$ZCS, 4 × 2 × 2 unit cells (relative to the fcc zincblende CdS unit cell, 4 Cd and 4 S atoms, respectively) with 128 atoms (with 1 Ni substitution) were used for the crystal structure and electronic structure calculations. We used the projector augmented wave potentials with 4s and 4p valence states for Cd, 3d, and 3s for Zn and Ni, and 3s and 3p for S with the cutoff energy of 500 eV. The conjugate gradient scheme is used to optimize the atom coordinates until the Hellmann-Feyman force is less than 0.01 eV $Å^{-1}$. The number of *k*-points was carefully optimized to achieve energy convergence, giving 2 × 2 × 2 and 1 × 2 × 2 Monkhorst-Pack BZ calculations for Ni_xZCS (x = 0.03125, 0.0625, and 0.125) and $Ni_{0.015625}$ZCS, respectively. To address the on-site Coulomb energy interactions in the localized d electrons of the transition metal ions (Ni, Zn, and Cd), an additional Hubbard-type *U* term was taken into account with the GGA + *U* approach (*49*). The *U* for Ni was fitted to be 5.7 eV. Free energy of different substitutional, interstitial Ni dispersion species as well as the consideration of the S and Cd vacancies in the presence of Ni impurities were calculated on the basis of the energy differences between the Ni-dispersed crystals, for example, $E_{\text{substituted Ni on Cd site of ZCS}} = E_{\text{NixZCS}} - E_{\text{ZCS}} - E_{n\text{-Ni}}$, where E_{NixZCS}, E_{ZCS}, and $E_{n\text{-Ni}}$ are the energies of the substituted Ni on Cd site of ZCS, ZCS, and Ni, respectively. Moreover, to identify the solubility of Ni in the ZCS solid solution, the formation energy of an impurity Ni is calculated on the basis of the following: $E_{f(\text{NixZCS})} = E_{\text{NixZCS}} - E_{\text{ZCS}} + \mu\text{Cd} - \mu\text{Ni}$, where E_{NixZCS} is the total energy of the supercell containing x Ni and E_{ZCS} is the total energy for the equivalent supercell containing only bulk ZCS. μCd and μNi are the chemical potentials of Cd and Ni, respectively, which satisfy the equilibrium constraint: $\mu\text{Cd} + \mu\text{S} \leq \mu_{\text{ZCS}}^{\text{bulk}}$, $\mu\text{S} \leq \mu_{\text{S}}^{\text{bulk}}$, and $\mu\text{Cd} \leq \mu_{\text{Cd}}^{\text{bulk}}$, where $\mu_{\text{ZCS}}^{\text{bulk}}$ is the energy of bulk ZCS. Under S-rich growth conditions here, the μS is calculated as the energy of one S atom in bulk α-S in the orthorhombic structure, then μCd is obtained by $\mu_{\text{ZCS}}^{\text{bulk}} - \mu\text{S}$. μNi is equal to the energy of one Ni atom in $NiCl_2$, as it was used here as the Ni precursor.

Surface calculations were conducted via a slab model with periodic boundary conditions. Both the orthorhombic nonpolar (110) surface and hexagonal polar (111) surfaces of the Ni_xZCS were cleaved from the relaxed Ni_xZCS (x = 0.03125, 0.0625, and 0.125) bulk crystals and built with a vacuum of about 20 Å and a five-layer slab of which the three bottom layers were kept fixed during relaxation. The surface energies and the adsorption energies were performed on the basis of the stoichiometric supercell models with 4 × 4 × 1 and 2 × 4 × 1 *k*-point meshes for Ni_xZCS (x = 0.03125, 0.0625, and 0.125) and $Ni_{0.015625}$ZCS slabs, respectively. The surface energies were obtained by the slab method

$$E_{\text{surface}} = (E_{\text{slab}} - \text{nE}_{\text{bulk}})/2nA$$

where A, E_{bulk}, and E_{slab} are the area of the supercell, the bulk energy per unit cell, and energy per surface unit cell of the specified slab model, respectively, and n is the number of bulk unit cells.

The OLA adsorption energy on (110) and (111) facets was calculated as follows

$$E_{\text{adsorption}} = -(E_{\text{slab + OLA}} - E_{\text{slab}} - E_{\text{OLA}})$$

where $E_{\text{slab+OLA}}$ is the energy of the adsorption complex including the relaxed surface and the OLA molecule, and E_{OLA} is the energy of OLA.

Here, the band structures of the bulk and (110) and (111) facets of Ni_xZCS (x = 0.015625, 0.03125, 0.0625, and 0.125) were calculated on the basis of the HSE06 hybrid functional (*50*) and the doped Ni_xZCS was compared with ZCS via the band unfolding technique. It recovers an effective primary cell picture of ZCS band structure from calculations using different supercells, including both intrinsic and extrinsic perturbations. The band unfolding calculations are carried out using the BandUP code (*51*).

The E_{CBM} and E_{VBM} versus vacuum edge positions of different facets were calculated on the basis of the calculated band structures and the relation between the bandgap (E_g), work function (Φ), and Fermi level (E_f): Work function (Φ) = $E_{(\text{vacuum})} - E_f$.

Reaction free energy

Three reactions were considered on (110) and (111) facets for evaluating their activities toward the HER and OER:

(i) H* adsorption at the cations (M = Ni, Zn, or Cd) or anion (S) sites (i.e., the Volmer reaction)

$$H^+ + e^- + *(\text{M or S}) \rightarrow H*(\text{M or S})$$

(ii) H_2O dissociation with HO* adsorbed at the cation or anion sites

$$H_2O + *(\text{M or S}) \rightarrow HO*(\text{M or S}) + H^+ + e^-$$

(iii) H_2O dissociation with O* adsorbed at the cation or anion sites

$$H_2O + *(\text{M or S}) \rightarrow O*(\text{M or S}) + 2H^+ + 2e^-$$

in which * represents an adsorption site on different facets of NixZCS QDs. Therefore, the final adsorption geometries in the above reactions were denoted as H*(M or S), HO*(M or S), and O*(M or S), respectively. The free energy for H* adsorption on each of the active sites of (110) and (111) facets [$\Delta G_{H^*(\text{M or S})}$] was calculated according to the following equation with determination of zero-point energy (ZPE) (ΔE_{ZPE}), entropy ($T\Delta S$), and the pH in solution [$\Delta G_{(\text{pH})}$] contributions

$$\Delta G_{H^*(\text{M or S})} = \Delta E_{H^*(\text{M or S})} + \Delta E_{\text{ZPE}} - T\Delta S - \Delta G_{(\text{pH})} + eU$$

where $\Delta E_{H^*(\text{M or S})}$ is the adsorption energy of an H* at the M or S site, which can be calculated with

$$\Delta E_{H^*(\text{M or S})} = (E_{\text{nH}^*} - E_{\text{slab}} - n \cdot E_{\text{H2}}/2)/n$$

in which the E_{slab}, E_{nH}*, and E_{H2} are the energies of the slab before and after adsorbing with nH* and an H_2 molecule, respectively. E_{H2} is the energy of hydrogen molecules in the gas phase. As the vibrational entropy of H* in the adsorbed state is small, the entropy of adsorption of $1/2H_2$ is the entropy of H_2 in the gas phase under standard conditions (*39*). $\Delta G_{(\text{pH})} = -kT\ln 10 \times \text{pH}$, where T is the temperature and k is the Boltzmann constant. U is the potential equivalent to the E_{CBM}, related to the effect of photoexcitation in photocatalysts. Non-Nernstian dependence of the sulfide band edges with a slope of 33 mV pH^{-1} has been considered (*52*). To determine the possible (110) and (111) surface terminations under the

photocatalytic conditions, the free energy for reactions (ii) and (iii) was calculated on the basis of the following equations

$$\Delta G_{\mathrm{HO^*(M\ or\ S)}} = \Delta E_{\mathrm{HO^*(M\ or\ S)}} + \Delta E_{\mathrm{ZPE}} - T\Delta S + \Delta G_{(\mathrm{pH})} - \mathrm{e}U$$

$$\Delta G_{\mathrm{O^*(M\ or\ S)}} = \Delta E_{\mathrm{O^*(M\ or\ S)}} + \Delta E_{\mathrm{ZPE}} - T\Delta S + 2\Delta G_{(\mathrm{pH})} - 2\mathrm{e}U$$

where ΔE_{HO}* and ΔE_{O}* are the adsorption energies of HO* and O* on (110) and (111) surfaces, which were calculated as the following equations

$$\Delta E_{\mathrm{HO^*(M\ or\ S)}} = (E_{\mathrm{nHO^*}} + n \cdot E_{\mathrm{H2}}/2 - E_{\mathrm{slab}} - n \cdot E_{\mathrm{H2O}})/n$$

$$\Delta E_{\mathrm{O^*(M\ or\ S)}} = (E_{\mathrm{nO^*}} + n \cdot E_{\mathrm{H2}} - E_{\mathrm{slab}} - n \cdot E_{\mathrm{H2O}})/n$$

E_{nHO}* and E_{nO}* are the energies of adsorption geometries HO*(M or S) and O*(M or S), respectively. E_{H2O} is the energy of a H_2O molecule.

SUPPLEMENTARY MATERIALS

Supplementary material for this article is available at http://advances.sciencemag.org/cgi/content/full/6/33/eaaz8447/DC1

REFERENCES AND NOTES

1. S. Wang, A. Y. Borisevich, S. N. Rashkeev, M. V. Glazoff, K. Sohlberg, S. J. Pennycook, S. T. Pantelides, Dopants adsorbed as single atoms prevent degradation of catalysts. *Nat. Mater.* **3**, 143–146 (2004).
2. B. Qiao, A. Wang, X. Yang, L. F. Allard, Z. Jiang, Y. Cui, J. Liu, J. Li, T. Zhang, Single-atom catalysis of CO oxidation using Pt1/FeO_x. *Nat. Chem.* **3**, 634–641 (2011).
3. L. Guan, X. Chen, Photoexcited charge transport and accumulation in anatase TiO_2. *ACS Appl. Energy Mater.* **1**, 4313–4320 (2018).
4. J. N. Tiwari, S. Sultan, C. W. Myung, T. Yoon, N. Li, M. Ha, A. M. Harzandi, H. J. Park, D. Y. Kim, S. S. Chandrasekaran, W. G. Lee, V. Vij, H. Kang, T. J. Shin, H. S. Shin, G. Lee, Z. Lee, K. S. Kim, Multicomponent electrocatalyst with ultralow Pt loading and high hydrogen evolution activity. *Nat. Energy* **3**, 773–782 (2018).
5. L. Cao, Q. Luo, W. Liu, Y. Lin, X. Liu, Y. Cao, W. Zhang, Y. Wu, J. Yang, T. Yao, S. Wei, Identification of single-atom active sites in carbon-based cobalt catalysts during electrocatalytic hydrogen evolution. *Nat. Catal.* **2**, 134–141 (2018).
6. D. Liu, X. Li, S. Chen, H. Yan, C. Wang, C. Wu, Y. A. Haleem, S. Duan, J. Lu, B. Ge, P. M. Ajayan, Y. Luo, J. Jiang, L. Song, Atomically dispersed platinum supported on curved carbon supports for efficient electrocatalytic hydrogen evolution. *Nat. Energy* **4**, 512–518 (2019).
7. J. Jiao, R. Lin, S. Liu, W.-C. Cheong, C. Zhang, Z. Chen, Y. Pan, J. Tang, K. Wu, S.-F. Hung, H. M. Chen, L. Zheng, Q. Lu, X. Yang, B. Xu, H. Xiao, J. Li, D. Wang, Q. Peng, C. Chen, Y. Li, Copper atom-pair catalyst anchored on alloy nanowires for selective and efficient electrochemical reduction of CO_2. *Nat. Chem.* **11**, 222–228 (2019).
8. H. Xu, D. Cheng, D. Cao, X. C. Zeng, A universal principle for a rational design of single-atom electrocatalysts. *Nat. Catal.* **1**, 339–348 (2018).
9. H. B. Yang, S.-F. Hung, S. Liu, K. Yuan, S. Miao, L. Zhang, X. Huang, H.-Y. Wang, W. Cai, R. Chen, J. Gao, X. Yang, W. Chen, Y. Huang, H. M. Chen, C. M. Li, T. Zhang, B. Liu, Atomically dispersed Ni (i) as the active site for electrochemical CO_2 reduction. *Nat. Energy* **3**, 140–147 (2018).
10. T. Wu, S. Sun, J. Song, S. Xi, Y. Du, B. Chen, W. A. Sasangka, H. Liao, C. L. Gan, G. G. Scherer, L. Zeng, H. Wang, H. Li, A. Grimaud, Z. J. Xu, Iron-facilitated dynamic active-site generation on spinel $CoAl_2O_4$ with self-termination of surface reconstruction for water oxidation. *Nat. Catal.* **2**, 763–772 (2019).
11. X. Zhang, D. Jing, M. Liu, L. Guo, Efficient photocatalytic H_2 production under visible light irradiation over Ni doped $Cd_{1-x}Zn_xS$ microsphere photocatalysts. *Catal. Commun.* **9**, 1720–1724 (2008).
12. X. Zhang, D. Jing, L. Guo, Effects of anions on the photocatalytic H_2 production performance of hydrothermally synthesized Ni-doped $Cd_{0.1}Zn_{0.9}S$ photocatalysts. *Int. J. Hydrog. Energy* **35**, 7051–7057 (2010).
13. Y. Wang, J. Wu, J. Zheng, R. Jiang, R. Xu, Ni^{2+}-doped $Zn_xCd_{1-x}S$ photocatalysts from single-source precursors for efficient solar hydrogen production under visible light irradiation. *Catal. Sci. Technol.* **2**, 581–588 (2012).
14. Z.-F. Huang, J. Song, Y. Du, S. Xi, S. Dou, J. M. V. Nsanzimana, C. Wang, Z. J. Xu, X. Wang, Chemical and structural origin of lattice oxygen oxidation in Co–Zn oxyhydroxide oxygen evolution electrocatalysts. *Nat. Energy* **4**, 329–338 (2019).
15. S. Yu, X.-B. Fan, X. Wang, J. Li, Q. Zhang, A. Xia, S. Wei, L.-Z. Wu, Y. Zhou, G. R. Patzke, Efficient photocatalytic hydrogen evolution with ligand engineered all-inorganic InP and InP/ZnS colloidal quantum dots. *Nat. Commun.* **9**, 4009 (2018).
16. H. Zhang, P. Zhang, M. Qiu, J. Dong, Y. Zhang, X. W. Luo, Ultrasmall MoO_x clusters as a novel cocatalyst for photocatalytic hydrogen evolution. *Adv. Mater.* **31**, 1804883 (2019).
17. R. K. Chava, J. Y. Do, M. Kang, Enhanced photoexcited carrier separation in CdS–SnS_2 heteronanostructures: A new 1D–0D visible-light photocatalytic system for the hydrogen evolution reaction. *J. Mater. Chem. A* **7**, 13614–13628 (2019).
18. S. Sun, H. Zeng, Size-controlled synthesis of magnetite nanoparticles. *J. Am. Chem. Soc.* **124**, 8204–8205 (2002).
19. Y. Yu, Q. Zhang, X. Lu, J. Y. Lee, Seed-mediated synthesis of monodisperse concave trisoctahedral gold nanocrystals with controllable sizes. *J. Phys. Chem. C* **114**, 11119–11126 (2010).
20. A. R. Denton, N. W. Ashcroft, Vegard's law. *Phys. Rev. A* **43**, 3161–3164 (1991).
21. Z. Quan, Z. Wang, P. Yang, J. Lin, J. Fang, Synthesis and characterization of high-quality ZnS, ZnS:Mn^{2+}, and ZnS:Mn^{2+}/ZnS (core/shell) luminescent nanocrystals. *Inorg. Chem.* **46**, 1354–1360 (2007).
22. A. Cao, Z. Liu, S. Chu, M. Wu, Z. Ye, Z. Cai, Y. Chang, S. Wang, Q. Gong, Y. Liu, A facile one-step method to produce graphene-CdS quantum dot nanocomposites as promising optoelectronic materials. *Adv. Mater.* **22**, 103–106 (2010).
23. R. S. C. Smart, W. M. Skinner, A. R. Gerson, XPS of sulphide mineral surfaces: Metal-deficient, polysulphides, defects and elemental sulphur. *Surf. Interface Anal.* **28**, 101–105 (1999).
24. H. Liu, Q. He, H. Jiang, Y. Lin, Y. Zhang, M. Habib, S. Chen, L. Song, Electronic structure reconfiguration toward pyrite NiS_2 via engineered heteroatom defect boosting overall water splitting. *ACS Nano* **11**, 11574–11583 (2017).
25. K. Gaskell, A. Starace, M. Langell, $Zn_xNi_{1-x}O$ rocksalt oxide surfaces: Novel environment for Zn^{2+} and its effect on the NiO band structure. *J. Phys. Chem. C* **111**, 13912–13921 (2007).
26. M. A. Peck, M. A. Langell, Comparison of nanoscaled and bulk NiO structural and environmental characteristics by XRD, XAFS, and XPS. *Chem. Mater.* **24**, 4483–4490 (2012).
27. R. J. O. Mossanek, I. Preda, M. Abbate, J. Rubio-Zuazo, G. Castro, A. Vollmer, A. Gutiérrez, L. Soriano, Investigation of surface and non-local screening effects in the Ni 2p core level photoemission spectra of NiO. *Chem. Phys. Lett.* **501**, 437–441 (2011).
28. S. Altieri, L. H. Tjeng, A. Tanaka, G. A. Sawatzky, Core-level x-ray photoemission on NiO in the impurity limit. *Phys. Rev. B* **61**, 13403–13409 (2000).
29. R. D. Leapman, L. A. Grunes, P. L. Fejes, Study of the L23 edges in the 3d transition metals and their oxides by electron-energy-loss spectroscopy with comparisons to theory. *Phys. Rev. B* **26**, 614–635 (1982).
30. D. Pearson, B. Fultz, C. Ahn, Measurements of 3d state occupancy in transition metals using electron energy loss spectrometry. *Appl. Phys. Lett.* **53**, 1405–1407 (1988).
31. T. Yamamoto, Assignment of pre-edge peaks in K-edge x-ray absorption spectra of 3d transition metal compounds: Electric dipole or quadrupole? *X-Ray Spectrom.* **37**, 572–584 (2008).
32. G. Rossi, F. d'Acapito, L. Amidani, F. Boscherini, M. Pedio, Local environment of metal ions in phthalocyanines: K-edge X-ray absorption spectra. *Phys. Chem. Chem. Phys.* **18**, 23686–23694 (2016).
33. A. A. Herzing, C. J. Kiely, A. F. Carley, P. Landon, G. J. Hutchings, Identification of active gold nanoclusters on iron oxide supports for CO oxidation. *Science* **321**, 1331–1335 (2008).
34. Q. Li, H. Meng, P. Zhou, Y. Zheng, J. Wang, J. Yu, J. R. Gong, $Zn_{1-x}Cd_xS$ Solid Solutions with Controlled Bandgap and Enhanced Visible-Light Photocatalytic H_2-Production Activity. *ACS Catal.* **3**, 882–889 (2013).
35. M. Thambidurai, N. Muthukumarasamy, S. Agilan, N. Murugan, N. S. Arul, S. Vasantha, R. Balasundaraprabhu, Studies on optical absorption and structural properties of Fe doped CdS quantum dots. *Solid State Sci.* **12**, 1554–1559 (2010).
36. J.-C. Wu, J. Zheng, P. Wu, R. Xu, Study of native defects and transition-metal (Mn, Fe, Co, and Ni) doping in a zinc-blende CdS photocatalyst by DFT and hybrid DFT calculations. *J. Phys. Chem. C* **115**, 5675–5682 (2011).
37. J. Yu, J. Low, W. Xiao, P. Zhou, M. Jaroniec, Enhanced photocatalytic CO_2-reduction activity of anatase TiO_2 by co-exposed {001} and {101} facets. *J. Am. Chem. Soc.* **136**, 8839–8842 (2014).
38. L. Li, P. A. Salvador, G. S. Rohrer, Photocatalysts with internal electric fields. *Nanoscale* **6**, 24–42 (2014).
39. Y. Jiao, Y. Zheng, K. Davey, S.-Z. Qiao, Activity origin and catalyst design principles for electrocatalytic hydrogen evolution on heteroatom-doped graphene. *Nat. Energy* **1**, 16130 (2016).
40. J. Schneider, D. W. Bahnemann, Undesired role of sacrificial reagents in photocatalysis. *J. Phys. Chem. Lett.* **4**, 3479–3483 (2013).

41. P. V. Kamat, S. Jin, Semiconductor photocatalysis: "Tell us the complete story!". *ACS Energy Lett.* **3**, 622–623 (2018).
42. H. A. Schwarz, Chain decomposition of aqueous triethanolamine. *J. Phys. Chem.* **86**, 3431–3435 (1982).
43. D. H. Pearson, C. C. Ahn, B. Fultz, White lines and d-electron occupancies for the 3d and 4d transition metals. *Phys. Rev. B* **47**, 8471–8478 (1993).
44. E. Patterson, C. Shelden, B. Stockton, Kubelka-Munk optical properties of a barium sulfate white reflectance standard. *Appl. Opt.* **16**, 729–732 (1977).
45. B. Ravel, M. Newville, ATHENA, ARTEMIS, HEPHAESTUS: Data analysis for X-ray absorption spectroscopy using IFEFFIT. *J. Synchrotron Radiat.* **12**, 537–541 (2005).
46. M. Newville, B. Ravel, D. Haskel, J. Rehr, E. Stern, Y. Yacoby, Analysis of multiple-scattering XAFS data using theoretical standards. *Phys. B Condens. Matter* **208**, 154–156 (1995).
47. L. Bugaev, V. Shuvaeva, I. Alekseenko, K. Zhuchkov, R. Vedrinskii, Determination of the local structure of NbO_6 octahedra in the orthorhombic phase of a $KNbO_3$ crystal using EXAFS. *Phys. Solid State* **40**, 1001–1005 (1998).
48. G. Kresse, J. Furthmüller, Efficient iterative schemes for ab initio total-energy calculations using a plane-wave basis set. *Phys. Rev. B* **54**, 11169–11186 (1996).
49. V. I. Anisimov, J. Zaanen, O. K. Andersen, Band theory and Mott insulators: Hubbard U instead of Stoner I. *Phys. Rev. B* **44**, 943–954 (1991).
50. J. Heyd, G. E. Scuseria, M. Ernzerhof, Hybrid functionals based on a screened Coulomb potential. *J. Chem. Phys.* **118**, 8207–8215 (2003).
51. P. V. C. Medeiros, S. Stafström, J. Björk, Effects of extrinsic and intrinsic perturbations on the electronic structure of graphene: Retaining an effective primitive cell band structure by band unfolding. *Phys. Rev. B* **89**, 041407 (2014).
52. T. Simon, N. Bouchonville, M. J. Berr, A. Vaneski, A. Adrovic, D. Volbers, R. Wyrwich, M. Doblinger, A. S. Susha, A. L. Rogach, F. Jackel, J. K. Stolarczyk, J. Feldmann, Redox shuttle mechanism enhances photocatalytic H_2 generation on Ni-decorated CdS nanorods. *Nat. Mater.* **13**, 1013–1018 (2014).
53. N. Tian, Z.-Y. Zhou, S.-G. Sun, Platinum metal catalysts of high-index surfaces: From single-crystal planes to electrochemically shape-controlled nanoparticles. *J. Phys. Chem. C* **112**, 19801–19817 (2008).
54. Y. Ding, Y. Gao, Z. L. Wang, N. Tian, Z.-Y. Zhou, S.-G. Sun, Facets and surface relaxation of tetrahexahedral platinum nanocrystals. *Appl. Phys. Lett.* **91**, 121901 (2007).
55. K. Yamaguchi, N. Mizuno, Efficient heterogeneous aerobic oxidation of amines by a supported ruthenium catalyst. *Angew. Chem. Int. Ed.* **42**, 1480–1483 (2003).
56. A. V. Naumov, I. V. Nechaev, T. V. Samofalova, V. N. Semenov, Structure and properties of thiocarbamide complexes of cadmium and zinc according to the results of a quantum-chemical calculation. *Russ. J. Appl. Chem.* **83**, 974–977 (2010).
57. J. W. Thomson, K. Nagashima, P. M. Macdonald, G. A. Ozin, From sulfur-amine solutions to metal sulfide nanocrystals: Peering into the oleylamine-sulfur black box. *J. Am. Chem. Soc.* **133**, 5036–5041 (2011).

Acknowledgments

Funding: This original research was supported by the Australia Research Council, Commonwealth of Australia, the Australian Renewable Energy Agency (ARENA), University of Technology Sydney (UTS), through the Discovery Early Career Researcher Award (DECRA DE170101009), ARC Discovery Project (DP170100436), ARENA 2014/RND106, UTS Chancellor's Postdoctoral Research Fellowship project (PRO16-1893), and UTS Early Career Researcher grant ECRGS PRO16-1304. We also acknowledge the use of the HAADF-STEM facility in the UOW Electron Microscopy Centre. **Author contributions:** D.W.S. conceived the research and carried out the synthesis, electrochemical tests, characterization, and the DFT calculations. J.R. performed the experimental measurements of photocatalysis. Z.W.Z. and C.C. conducted the x-ray absorption spectroscopy. Y.D.L., S.Z.Q., and G.X.W. discussed the overall research. D.W.S. conceived the project and drafted the manuscript. All authors discussed the experiments and the final manuscript. **Competing interests:** The authors declare that they have no competing interests. **Data and materials availability:** All data needed to evaluate the conclusions in the paper are present in the paper and/or the Supplementary Materials. Additional data related to this paper may be requested from the authors.

Submitted 14 October 2019
Accepted 2 July 2020
Published 14 August 2020
10.1126/sciadv.aaz8447

Citation: D. W. Su, J. Ran, Z. W. Zhuang, C. Chen, S. Z. Qiao, Y. D. Li, G. X. Wang, Atomically dispersed Ni in cadmium-zinc sulfide quantum dots for high-performance visible-light photocatalytic hydrogen production. *Sci. Adv.* **6**, eaaz8447 (2020).

Science Advances

Atomically dispersed Ni in cadmium-zinc sulfide quantum dots for high-performance visible-light photocatalytic hydrogen production

D. W. Su, J. Ran, Z. W. Zhuang, C. Chen, S. Z. Qiao, Y. D. Li and G. X. Wang

Sci Adv **6** (33), eaaz8447.
DOI: 10.1126/sciadv.aaz8447